Application of Matched Statistical Filters for EarthCARE Cloud Doppler Products

Ousmane O. Sy, Simone Tanelli, Pavlos Kollias, and Yuichi Ohno

***Abstract*—This paper presents a method for filtering the random noise that affects spaceborne Doppler measurements of atmospheric velocities. The proposed method hinges on adaptive low-pass filters that apply to the measured pulse-pair correlation function. The parameters of the filters are found by optimizing the statistics of the velocity residue of the filter. The method is illustrated by simulations of the cloud-profiling radar of the future Earth Cloud, Aerosol and Radiation Explorer (EarthCARE) mission of the European Space Agency and the Japanese Space Exploration Agency. These simulations, which do not include strong convection, show the higher performance of the filters when compared with the traditional increase of the along-track integration length. The results obtained with the filters show that velocity accuracies of 0.48, 0.42, and 0.39 $\mathrm{m \cdot s^{-1}}$ are achievable at PRF $= \{6.1, 7, 7.5\}$ kHz, respectively, while preserving the initial 500-m sampling of the measured EarthCARE data. These results also show the potential benefits of avoiding excessive along-track integration, for postprocessing tasks such as dealiasing or the retrieval of the vertical distribution of the atmospheric velocity (e.g., longer than 5 km for cases consistent with the climatologies represented in this data set).**

***Index Terms*—Entropy, matched filters, pulse Doppler radar, random noise, spaceborne radar.**

I. Introduction

THE launch in 2016 of the Earth Cloud, Aerosol and Radiation Explorer (EarthCARE) mission will put in orbit the first spaceborne W-band (94 GHz) radar with Doppler capability. The EarthCARE cloud profiling radar (CPR), henceforth denoted EC-CPR, will observe cloud and precipitation processes in the atmosphere by measuring their reflectivity and mean vertical velocity on a global scale. The EarthCARE measurements will serve both operational and research purposes by enabling the distinction between stratiform and convective scenes, by quantifying energy and heat transfers, or by improving the microphysical characterization of clouds and precipitation [1].

Manuscript received August 29, 2013; revised January 15, 2014 and February 23, 2014; accepted February 28, 2014. Date of publication April 16, 2014; date of current version May 30, 2014.

O. O. Sy and S. Tanelli are with the Radar Science and Engineering Department, Jet Propulsion Laboratory, California Institute of Technology, Pasadena, CA 91109 USA (e-mail: ousmane.o.sy@jpl.nasa.gov; simone.tanelli@jpl.nasa.gov).

P. Kollias is with McGill University, Montreal, QC H3A 0G4, Canada (e-mail: pavlos.kollias@mcgill.ca).

Y. Ohno is with the National Institute of Information and Communication Technology, Koganei 184-8795, Japan (e-mail: ohno@nict.go.jp).

Color versions of one or more of the figures in this paper are available online at http://ieeexplore.ieee.org.

Digital Object Identifier 10.1109/TGRS.2014.2311031

TABLE I
CHARACTERISTICS OF THE EARTHCARE CPR [21]

Parameter	Symbol	EarthCARE
Spacecraft altitude	h_{SAT}	400 km
Orbit inclination	θ_{orbit}	97°
Projected spacecraft velocity	V_{SAT}	$7.2\ \mathrm{km \cdot s^{-1}}$
Frequency	f	94.05 GHz
Pointing angle		Nadir
Beamwidth	θ_3	0.095°
Pulse duration	τ	3.3 μs
Pulse-repetition frequency (PRF)	f_{S}	[6.1, 7.5] kHz
Number of active pulses per burst	N_{pulse}	22
Number of silent pulses per burst	N_{gap}	2

Given the configuration of EarthCARE, which is detailed in Table I, the CPR will have to overcome various challenges to accurately measure Doppler velocities using a pulse-pair (PP) estimator [2]. Due to the low-Earth orbit of EarthCARE, the large projected instantaneous velocity of the spacecraft ($V_{\mathrm{SAT}} = 7.2\ \mathrm{km \cdot s^{-1}}$) will act as shear and broaden the Doppler spectrum perceived from the spacecraft. This will induce a temporal decorrelation of the received radar signal, which, in turn, will increase the amplitude of random fluctuations in the PP velocity estimate [1], [3]. The spectral broadening also enhances nonuniform beam-filling (NUBF) biases in the measured velocity [4], [5]. Furthermore, aliasing and multiple-scattering issues, unavoidable in regions of high precipitation or convection, and hardware-induced drifts and platform-motion biases will increase the uncertainty of the mean Doppler velocity estimates [3], [6].

Until the launch of EarthCARE, numerical simulations are the only means to investigate the performance of EC-CPR. These simulations can be done starting from either numerical products of cloud-resolving models or from actual W-band Doppler measurements acquired from a ground-based or airborne platform. Following this principle, various methods have been proposed to detect and correct for multiple-scattering problems [7], NUBF errors [4], [5], aliasing [8], pointing inaccuracies [6], or random-fluctuation problems [9]. Focusing on the latter, the common solution consists in performing a longer onboard integration of the radar echoes, i.e., increasing the number of radar pulses that are used in the PP estimation of the Doppler reflectivity and velocity [3]. Due to the correlation that exists between radar returns, the reduction in the variance of the velocity estimate is generally smaller than the theoretical variance reduction achievable by integrating mutually statistically independent radar pulses [10]. However, the longer integration comes at the cost of a coarser spatial sampling of the final radar

product, which raises the issue of the representativeness and practical usefulness of the integrated data [9].

The aim of this paper is to address the issue of the random fluctuations of the measured mean Doppler velocity, whereas the NUBF and aliasing were addressed in [8]. Instead of the traditional constant integration, we propose to apply an adaptive low-pass filter to the Fourier spectrum of the pulse-to-pulse correlation function, from which the filtered mean velocity is deduced by PP processing. Working with the spectrum of the correlation function circumvents possible aliasing problems that occur when using the mean velocity. The characteristics of the optimal filter are obtained by applying various optimization schemes to the statistical parameters of the filtered velocity field.

First, to highlight the potential of the filtering approach, we begin by assuming that the true velocity field is known. As a result, the optimal filter can be identified as the one that minimizes the root-mean-square (RMS) error between the measured velocity and the true velocity. In a second stage, more practical approaches are proposed, which only rely on the measured velocity and on the velocity residue, i.e., the difference between the prefiltering and filtered velocity fields, both of which are available in operational conditions. The first filter of this type is one that maximizes the entropy of the residue, following a statistical or thermodynamic rationale. As an alternative, a constructive approach is proposed, which seeks the optimal filter as the one that leads to the statistical independence between the prefiltering and filtered velocity errors. This scheme then leads to target values for the probability distribution of the velocity residue. These target values are analytically estimated by simulating a Doppler spectrum centered about 0 $\mathrm{m}\cdot\mathrm{s}^{-1}$ and with a width consistent with the characteristics of EC-CPR.

The outline of this paper is as follows. Section II presents the general method used to simulate EarthCARE Doppler data using high-resolution measurements obtained either from a ground-based or an airborne instrument. The traditional onboard integration method is then discussed in Section III, where its shortcomings are illustrated through the example of a snowstorm event recorded in Wakasa Bay, Japan, in 2003. Next, the filtering process that we propose is explained in Section IV, where the optimization of the filter parameters is also outlined. Section V then provides results obtained for the snowstorm case of Wakasa Bay, in Section V-A, and general statistics drawn from the analysis of a large set of EC-CPR simulations, in Section V-B.

II. Spaceborne Doppler Simulations Using High-Resolution Data

Due to the absence of actual spaceborne Doppler measurements, the products of EC-CPR are simulated using nonspaceborne Doppler data. The broad lines of the simulation method, which is explained in extenso in [8], are recalled here. Owing to the nonscanning character of EC-CPR and its small beamwidth, the configuration is parametrized in the orbital plane where any point $\boldsymbol{M}(x,h)$ is referenced by its along-track coordinate x and its height h above the ground [3]. For instance, the spacecraft is assumed to be located at the point $\boldsymbol{M}_{\mathrm{SAT}}(x_{\mathrm{SAT}},h_{\mathrm{SAT}})$, as shown in Fig. 1.

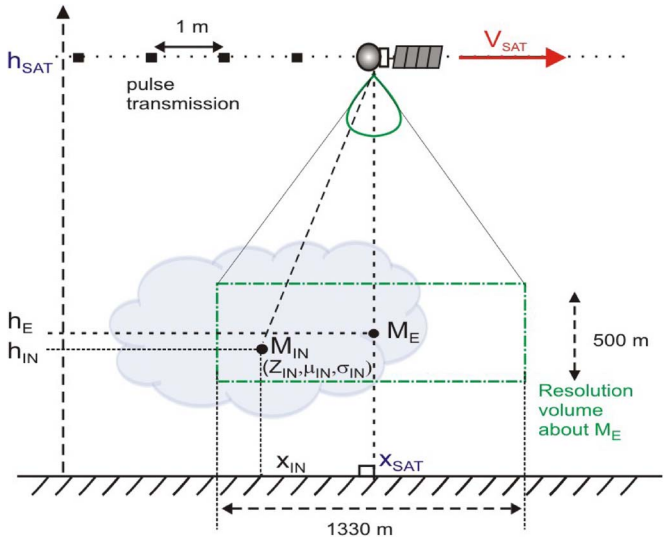

Fig. 1. Instantaneous configuration: EC-CPR located at $\boldsymbol{M}_{\mathrm{SAT}}(x_{\mathrm{SAT}}, h_{\mathrm{SAT}})$, resolution volume $\mathcal{V}(\boldsymbol{M}_{\mathrm{E}})$ centered around $\boldsymbol{M}_{\mathrm{E}}(x_{\mathrm{E}},h_{\mathrm{E}})$ and containing points $\boldsymbol{M}_{\mathrm{IN}}(x_{\mathrm{IN}},h_{\mathrm{IN}})$, where the Doppler data $(Z_{\mathrm{IN}},\mu_{\mathrm{IN}},\sigma_{\mathrm{IN}})$ $(\boldsymbol{M}_{\mathrm{IN}})$ are known.

The input data consist of measurements of reflectivity factors Z_{IN}, mean vertical velocities μ_{IN}, and spectral widths σ_{IN}. These measurements are acquired by ground-based and airborne radars operating at the same frequency as EC-CPR, i.e., ~95 GHz, but at a higher spatial resolution than EC-CPR. Using these data, the Doppler power spectrum P_{IN} of each elementary volume is approximated by a Gaussian.

Given a point $\boldsymbol{M}_{\mathrm{E}}(x_{\mathrm{E}},h_{\mathrm{E}})$, where $x_{\mathrm{E}}=x_{\mathrm{SAT}}$, and h_{E} is the height of a range gate of EC-CPR, the volume of resolution about $\boldsymbol{M}_{\mathrm{E}}$ has horizontal and vertical dimensions given by the supports $\mathcal{X}$ and $\mathcal{H}$ of the two-way antenna pattern f_{X} and the range-weighting function f_{H}, respectively.

To obtain a reference against which EC-CPR simulations can be compared, the input Doppler spectra are averaged using f_{X} and f_{H} as follows:

$$P_{\mathrm{TRUE}}(\boldsymbol{M}_{\mathrm{E}},v)=\int_{\mathcal{H}}\omega_{\mathrm{H}}(h_{\mathrm{IN}}-h_{\mathrm{E}})\int_{\mathcal{X}}\omega_{\mathrm{X}}(x_{\mathrm{IN}}-x_{\mathrm{E}})\times P_{\mathrm{IN}}(x_{\mathrm{IN}},h_{\mathrm{IN}},v)dx_{\mathrm{IN}}\,dh_{\mathrm{IN}} \quad (1)$$

where the normalized weighting functions ω_{X} and ω_{H} are defined as

$$\omega_{\mathrm{X}}(x)=\frac{f_{\mathrm{X}}(x)}{\int_{\mathcal{X}}f_{\mathrm{X}}(x')\,dx'}\ \text{for any}\ x\in\mathcal{X}$$

$$\omega_{\mathrm{H}}(h)=\frac{f_{\mathrm{H}}(h)}{\int_{\mathcal{H}}f_{\mathrm{H}}(h')\,dh'}\ \text{for any}\ h\in\mathcal{H}. \quad (2)$$

The zeroth- and first-order moments of P_{TRUE} are the reflectivity factor Z_{TRUE} and the mean velocity μ_{TRUE}, which are taken as the truth.

The actual Doppler spectrum P_{E}, as seen by EC-CPR, is obtained by shifting the mean of the input spectra by the projection of the spacecraft velocity vector $\boldsymbol{V}_{\mathrm{SAT}}$ across the footprint and then summing these shifted spectra according to the antenna

weighting functions as in (1). The resulting Doppler power spectrum P_{E} includes the effect of the spacecraft-induced spectral broadening [11], as well as NUBF velocity biases when the reflectivity is not symmetrically distributed within the resolution volume [4]. Although P_{IN} is approximated by a Gaussian, similarly to what is done in kernel density estimation [12], the composite spectra P_{TRUE} and P_{E} will have any arbitrary shapes allowed by (1), not necessarily a Gaussian shape. Next, a stochastic Fourier method [13] is applied to P_{E} to derive the time series of complex-voltage samples ((I, Q) samples). The resulting stochastic (I, Q) samples, which are denoted $\{V_{\boldsymbol{M}_{\mathrm{E}}}(k\ T_s)$, for $k = 1, \ldots, N_{\mathrm{pulse}}\}$, are sampled at the rate of the PRF $1/T_{\mathrm{S}}$ and include the effects of the random distribution of the atmospheric scatterers, the finite PRF, and the vertical oversampling of EC-CPR [8].

The single-burst PP estimates of the reflectivity, i.e., $Z_{\mathrm{PP},1}$, and of the mean velocity, i.e., $\mu_{\mathrm{PP},1}$, read

$$Z_{\mathrm{PP},1}(\boldsymbol{M}_{\mathrm{E}}) = \sum_{\ell=1}^{N_{\mathrm{pulse}}} |V_{\boldsymbol{M}_{\mathrm{E}}}(\ell T_s)|^2 \tag{3}$$

$$\mu_{\mathrm{PP},1}(\boldsymbol{M}_{\mathrm{E}}) = \frac{V_{\mathrm{Nyq}}}{\pi} \arg\left[K_{\mathrm{PP},1}(\boldsymbol{M}_{\mathrm{E}})\right] \tag{4}$$

where $V_{\mathrm{Nyq}} = \lambda/(4T_{\mathrm{S}})$ is the Nyquist velocity, λ is the wavelength of EC-CPR, and $K_{\mathrm{PP},1}$ is the lag-1 correlation function given by

$$K_{\mathrm{PP},1}(\boldsymbol{M}_{\mathrm{E}}) = \sum_{\ell=1}^{N_{\mathrm{pulse}}-1} V^*_{\boldsymbol{M}_{\mathrm{E}}}[\ell T_s] \times V_{\boldsymbol{M}_{\mathrm{E}}}\left[(\ell+1)T_s\right] \tag{5}$$

with $V^*_{\boldsymbol{M}_{\mathrm{E}}}$ being the complex conjugate of $V_{\boldsymbol{M}_{\mathrm{E}}}$.

To mitigate the effects of the random noise on the EC-CPR Doppler products, contiguous burst groups are integrated along track, on a range-bin-by-range-bin basis. In doing so, $N_{\mathrm{gap}} = 2$ "silent" pulses are included between consecutive bursts of (I, Q) samples. Assuming that N_{integ} consecutive burst groups are integrated, the resulting Doppler moments are computed using $N_{\mathrm{integ}} N_{\mathrm{pulse}}$ voltage samples in the PP formulas (3)–(5). The thus obtained PP estimates of the reflectivity and mean velocity are denoted Z_{PP} and μ_{PP}, respectively. As a result, the variances of Z_{PP} and μ_{PP} are reduced by a factor N_{integ}, in the best case, i.e., if the bursts are mutually statistically independent. The tradeoff for the reduced uncertainty of Z_{PP} and μ_{PP} is a N_{integ} times coarser horizontal sampling. On board EC-CPR, a 500-m integration will be performed to produce the "level-1B" Doppler data. This amounts to integrating approximately 18 (22) burst groups at PRF$=6.1$ kHz(PRF$=7.5$ kHz).

III. Accuracy of the EC-CPR Mean Velocity

By neglecting hardware-induced or platform stability errors, the mean velocity estimate μ_{PP} is mainly affected by aliasing, NUBF, and random-fluctuation errors (discussed in Section II), as well as multiple scattering.

The aliasing errors are caused by the function $\arg(\cdot)$ in (4), which limits the value of μ_{PP} to the range $[-V_{\mathrm{Nyq}}, +V_{\mathrm{Nyq}}]$. Owing to the organized spatial patterns in which aliasing errors appear, μ_{PP} can be unwrapped using a near-neighbor dealiasing logic [10]. However, with EC-CPR Doppler measurements, the random noise is generally spatially uncorrelated (or it has a correlation length that is shorter than the spatial sampling of the PP data), and it can therefore produce large variations of μ_{PP} over a short distance [8]. Due to these large random errors of μ_{PP} (given the operational parameters), Doppler folding should be expected not only when the Doppler velocities exceed the Nyquist boundaries but also due to the random noise. This is expected to make the application of traditional near-neighbor unfolding algorithms challenging. Alternative methods include mapping techniques [14] or educated dealiasing algorithms if a reference velocity map is available, e.g., through a different channel or instrument.

The NUBF velocity errors are caused by inhomogeneities of the reflectivity in the along-track direction within the resolution volume of the CPR. These errors can be efficiently corrected for using their correlation to the along-track gradient of Z_{PP} [4], [8]. The correction is all the more efficient as the horizontal sampling of Z_{PP} is finer to be representative of the subbeam variations. However, this requirement of a finer along-track sampling partly contradicts the principle of a longer along-track integration to reduce the random noise. In the particular case of EC-CPR, since the level 1B data are sampled every 500 m, the along-track gradient can be computed by central finite differences over a 1-km baseline, which is very close to the length of the projected 3-dB antenna pattern, i.e., $\sim$800 m. Therefore, depending on the severity of the NUBF biases, the gradient-based correction will only overcome NUBF errors partially.

Where multiple scattering affects the radar return, both the reflectivity and the mean Doppler velocity lose their direct connection to the single-scattering interpretation [7], [15]. Depending on the severity of the multiple-scattering contamination, the corresponding errors can significantly reduce the portion of usable radar profile. Multiple scattering is expected to be particularly significant in deep convection and heavy precipitation, which are extreme regimes not analyzed in this paper.

Once other errors have been accounted for, the residual velocity error is due to the random noise and to the finite radar sampling. Just as in ground-based Doppler weather radars, this noise is caused by the loss of phase coherence between consecutive (I, Q) samples, which stems from the relative motion of the hydrometeors included in the radar volume of resolution, and from thermal noise. Moreover, the large instantaneous speed of the spacecraft induces spectral broadening, which further decorrelates the consecutive radar returns [3]. The common solution to this problem consists in increasing the integration time. For instance, the "level-2" products of EC-CPR will be obtained by integrating over 1 and 10 km [16].

A. Illustration of the Effects of a Longer Along-Track Integration

To illustrate the effects of the along-track integration on the accuracy of the Doppler data, we consider EC-CPR simulations performed using airborne measurements recorded by the W-band SPIDER radar of the National Institute of Information and Communications Technology (NICT), in Japan [17]. The spaceborne Doppler products are simulated by approximating the two-way antenna pattern as a Gaussian pencil beam [3]

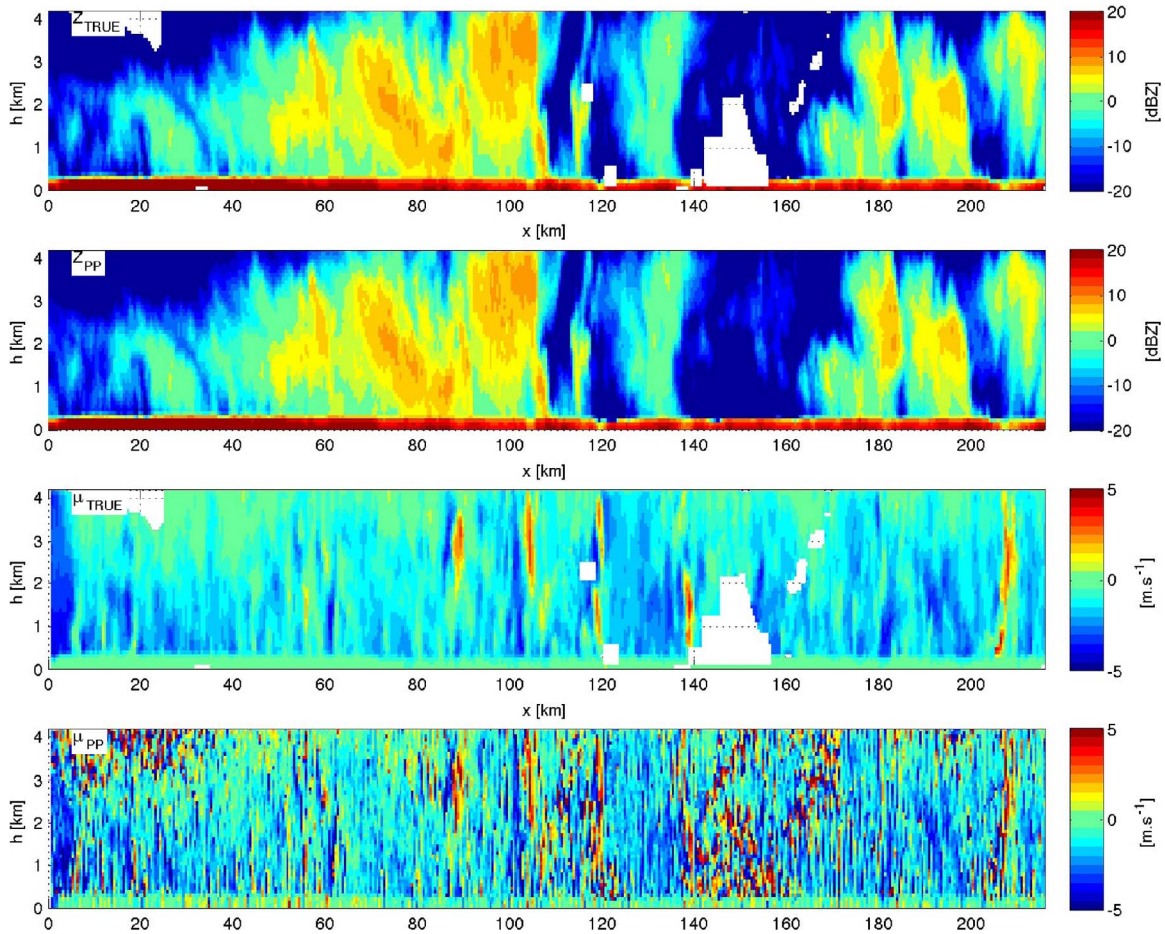

Fig. 2. Snowstorm measured by SPIDER: true reflectivity Z_{TRUE} averaged at the (top row) EarthCARE resolution, (second row) realistic reflectivity Z_{PP} estimated by PP processing, (third row) true mean velocity μ_{TRUE} averaged at the EarthCARE resolution, and (bottom row) realistic mean velocity μ_{PP} estimated by PP processing.

and for PRF $= 7$ kHz, which is an intermediate value between the limit values of EC-CPR's PRF, viz., PRF $= 6.1$ kHz and PRF $= 7.5$ kHz. The event displayed in Fig. 2 corresponds to a snowstorm measured by SPIDER on January 29, 2003. This test case involves large spatial variations of the reflectivity and the mean velocity.

As expected from EC-CPR's specifications, the measured reflectivity Z_{PP} is very accurate (RMS error of $\sim$0.3 dB for SNR ≥ 6). The PP estimated velocity μ_{PP} displayed in Fig. 2 (row 4) is corrected for NUBF as in [8]. Despite the random fluctuations, μ_{PP} captures the features of μ_{TRUE}, such as the localized convective areas located around $x \in \{90, 105, 120, 140, 208\}$ km. The well-known dependence on SNR [2] is particularly evident in regions with negative SNR (i.e., below -21.5 dBZ for EC-CPR), where μ_{PP} estimates assume almost a uniform distribution within the Nyquist interval. However, the random fluctuations of the PP estimate are also clearly visible at the surface where μ_{PP} has nonvanishing values, although $|\mu_{\mathrm{TRUE}}| \sim 0$ m $\cdot$ s^{-1} and SNR $\gg 0$ dB. Prior to any velocity filtering, the RMS velocity error is $\sigma_{\mathrm{PRE}} = 1.38$, 1.27, and 1.19 m $\cdot$ s^{-1} for SNR ≥ 1.5, SNR ≥ 6, and SNR ≥ 16.5 (corresponding to $Z_{\mathrm{PP}} \geq -20$ dBZ, $Z_{\mathrm{PP}} \geq -15.5$ dBZ, and $Z_{\mathrm{PP}} \geq -5$ dBZ), respectively.

The error reduction achieved by a longer along-track integration is illustrated in Fig. 3 for integration lengths of 1, 5, and 10 km. As expected, increasing the integration length reduces the amplitude of the random fluctuations in μ_{PP}. This improvement can be quantified in the RMS sense by comparing the integrated μ_{PP} to the average of μ_{TRUE} at the same integrated horizontal spacing, as shown in Table II. The gain in accuracy is slightly smaller than the hypothetical improvement expected when independent profiles are integrated, i.e., an RMS error reduction by a factor $\sqrt{N_{\mathrm{integ}}}$ [2].

However, Fig. 3 also shows how an excessive integration can lead to the loss of fine-scale information initially present in μ_{TRUE}. This can be quantified by comparing the integrated μ_{PP} to the true velocity μ_{TRUE} at the original level-1B sampling of 500 m. To measure this effect, the integrated velocity μ_{PP} is first interpolated down to the 500-m sampling.

The results obtained after near-neighbor and linear interpolation are shown in Table II. While the linear interpolation produces slightly more accurate results than the near-neighbor interpolation, particularly for the 1-km data, the improvement in performance is minor. Furthermore, excessively integrated data, e.g., over lengths larger than 5 km, fail to capture the dynamic of the true signal μ_{TRUE}, hence the RMS error of $\sim$0.95 m $\cdot$ s^{-1}, which is mainly due to the dynamic or energy of μ_{TRUE} that was eliminated by filtering. It is evident, for example, how the four convective cells have almost entirely disappeared from these excessively integrated velocities.

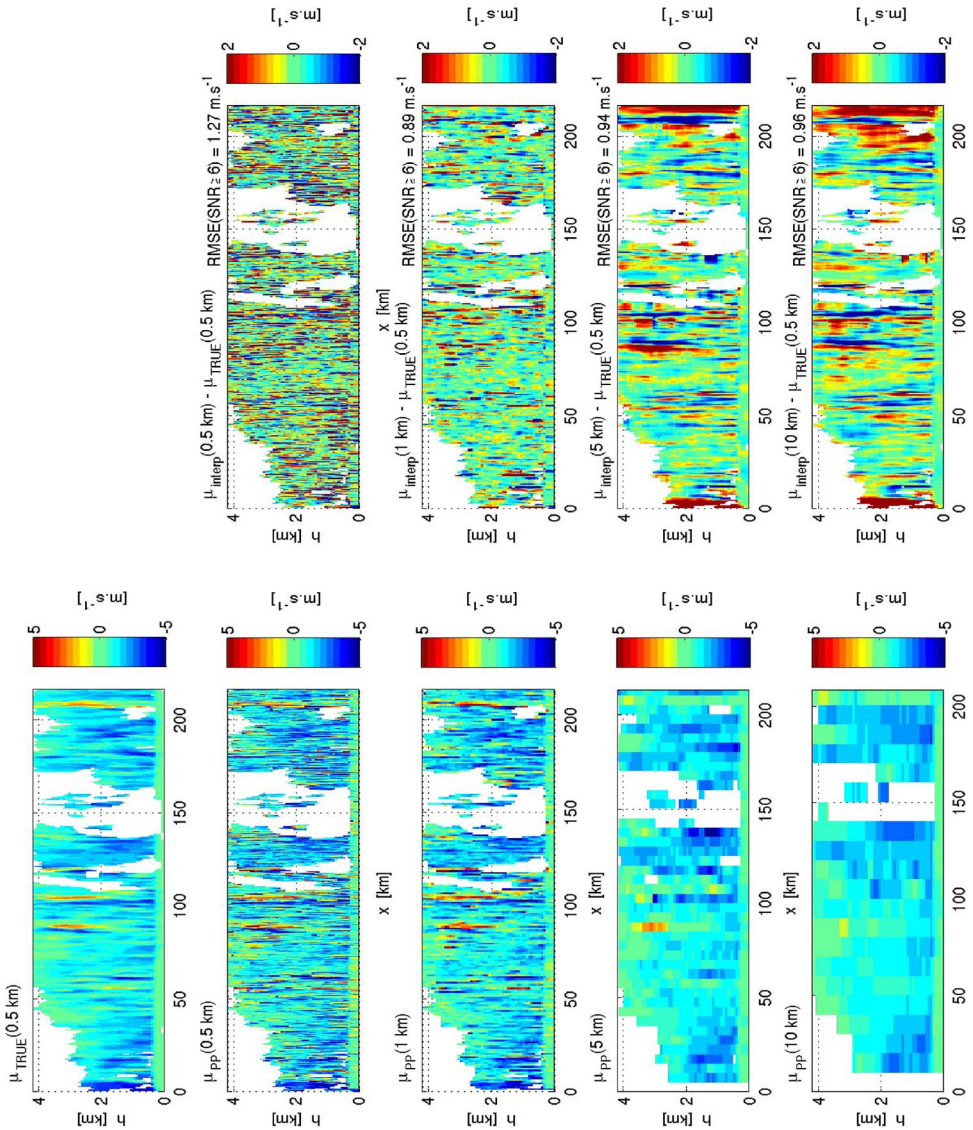

Fig. 3. Snowstorm measured by SPIDER: effect of a longer along-track integration on the (left) PP velocity and (right) its error for SNR ≥ 6. Results are shown for the (first row) reference velocity μ_{TRUE}, the (second row) level-1B PP velocity μ_{PP}, and longer along-track integrations, viz., (third row) 1 km, (fourth row) 5 km, and (fifth row) 10 km.

TABLE II
EFFECT OF A LONGER ALONG-TRACK INTEGRATION ON THE ACCURACY OF μ_{PP} FOR SNR ≥ 6: RMS ERROR BETWEEN THE INTEGRATED μ_{PP} AND THE HORIZONTALLY AVERAGED μ_{TRUE} (SECOND AND THIRD COLUMNS); RMS ERROR BETWEEN THE INTEGRATED μ_{PP} INTERPOLATED TO THE LEVEL-1B AND THE LEVEL-1B μ_{TRUE} (FOURTH AND FIFTH COLUMNS)

Integration	RMS of error vs averaged μ_{TRUE} $[\mathrm{m}\cdot\mathrm{s}^{-1}]$		RMS of error vs 500 m μ_{TRUE} $[\mathrm{m}\cdot\mathrm{s}^{-1}]$	
length	measured	theoretical	after NN interpolation	after linear interpolation
500 m	1.27	1.27	1.27	1.27
1 km	0.97	0.90	1.16	0.89
5 km	0.51	0.40	1.00	0.94
10 km	0.30	0.28	1.01	0.96

IV. ADAPTIVE LOW-PASS FILTERING

A. Spectrum of the Pulse Pair Correlation Function

The along-track integration performed by EC-CPR to obtain the profiles of vertical velocity is now analyzed in the spectral domain. To begin with, we consider the correlation function K_{PP} of level-1B PP, which is defined in (5). Starting the reasoning with the correlation function has the advantage of avoiding aliasing issues. At this stage, we also assume that NUBF errors have been corrected by using, for instance, a reflectivity gradient method, i.e.,

$$K(x_{\mathrm{E}},h_{\mathrm{E}}) = K_{\mathrm{PP}}(x_{\mathrm{E}},h_{\mathrm{E}})\exp\left[-j\pi\frac{\kappa_{\mathrm{NUBF}}\nabla_x Z_{\mathrm{PP}}(x_{\mathrm{E}},h_{\mathrm{E}})}{V_{\mathrm{Nyq}}}\right] \tag{6}$$

where κ_{NUBF} is chosen as $\kappa_{\mathrm{NUBF}} = 0.195\ \mathrm{m}\cdot\mathrm{s}^{-1}\cdot(\mathrm{dB}\cdot\mathrm{km}^{-1})^{-1}$ [8].

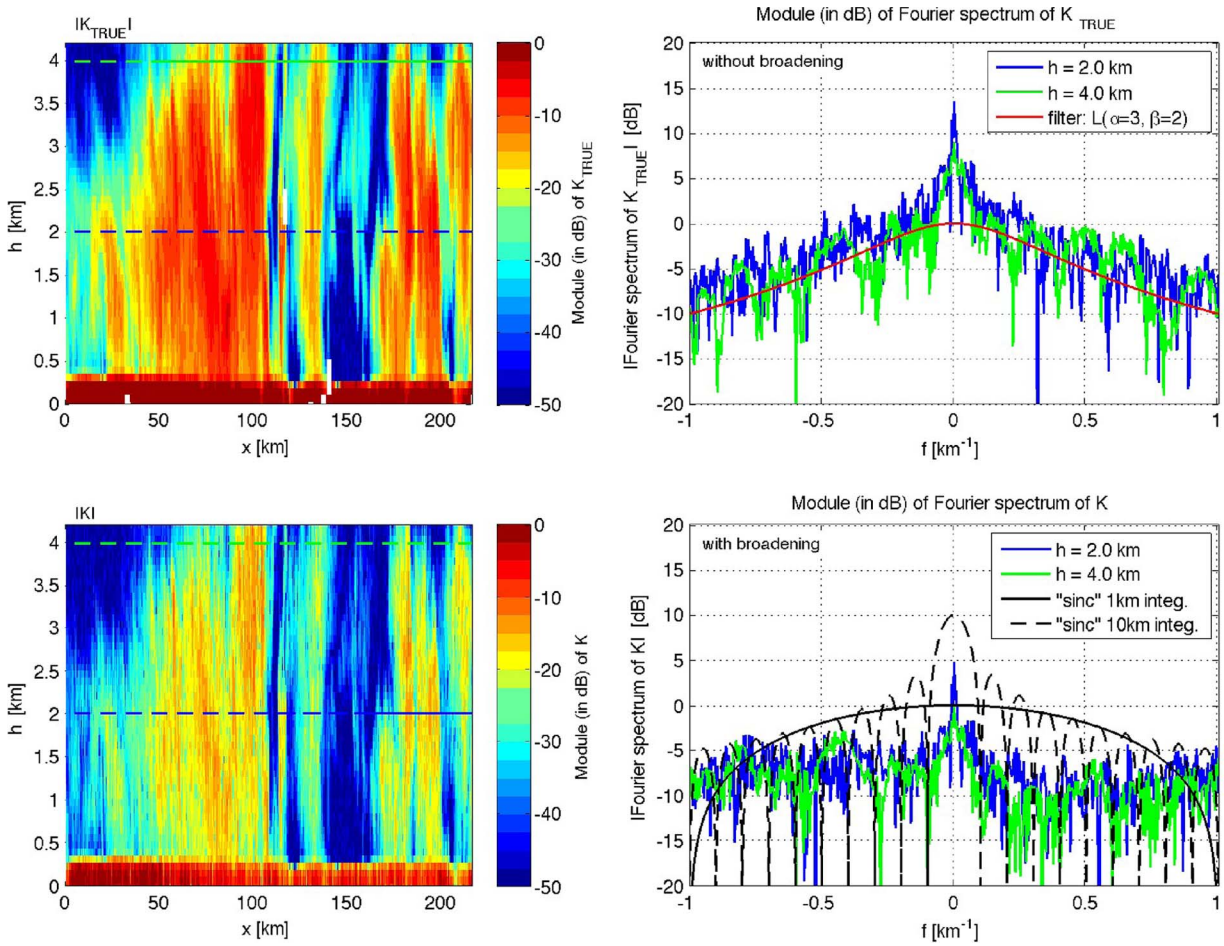

Fig. 4. Snowstorm measured by SPIDER: amplitudes of (top left) K_{TRUE} and (bottom left) K and amplitudes of the Fourier transforms (top right) $\mathcal{K}_{\mathrm{TRUE}}$ and (bottom right) $|\mathcal{K}|$ at the range gates $h = 2$ km and $h = 4$ km. The (top right) low-pass filter $\mathcal{L}_{\alpha=3,\beta=2}$ and the (bottom right) "sinc" filters corresponding to 1 and 10 km along-track integrations are also plotted.

We first consider a data set comprising N_{X} radar profiles spaced every $\Delta_{\mathrm{X}} = 500$ m along track and N_{H} range gates spaced every $\Delta_{\mathrm{H}} = 100$ m.

Let $\mathcal{K}$ denote the along-track Fourier transform of K, i.e.,

$$\mathcal{K}(f, h_{\mathrm{E}}) = \int_{\mathbb{R}} e^{-j2\pi f x_{\mathrm{E}}} K(x_{\mathrm{E}}, h_{\mathrm{E}})\, dx_{\mathrm{E}} \quad \forall f \in \mathbb{R}. \tag{7}$$

The discrete sampling of K implies that $\mathcal{K}$ is available over the bandwidth $[-(2\Delta_{\mathrm{X}})^{-1}, (2\Delta_{\mathrm{X}})^{-1}]$ and sampled at the rate $\Delta f = (N_{\mathrm{X}}\Delta_{\mathrm{X}})^{-1}$. Since K is complex valued, $\mathcal{K}$ will generally be nonsymmetrical with respect to the origin $f = 0$ km^{-1}.

As an example, the amplitude of the PP correlation function K is shown in Fig. 4 for the snowstorm case discussed in Section III-A. To serve as a reference, the PP correlation function K_{TRUE} of the true signal, i.e., unaffected by the spacecraft-induced spectral broadening, is also plotted. The weakness of $|K|$ compared with $|K_{\mathrm{TRUE}}|$ is due to the temporal decorrelation between consecutive EC-CPR voltage samples. In Fig. 4, a comparison between $|\mathcal{K}_{\mathrm{TRUE}}|$ and $|\mathcal{K}|$, which are plotted for the range gates $h = 2$ km and $h = 4$ km, illustrates the spectral impact of the Doppler broadening: while $|\mathcal{K}_{\mathrm{TRUE}}|$ is a slowly decaying function of $|f|$ with a clearly defined mode in the low $|f|$ region, instead, the random fluctuations and the spacecraft-induced spectral broadening whiten the spectrum $\mathcal{K}$, thereby reducing the SNR to levels close to zero, even in the low-frequency regions. To overcome this issue, a rectifying or matching filter needs to be applied to restore the shape of the spectrum.

An along-track integration of the level-1B data by a factor N_{integ} is equivalent to a uniform horizontal averaging of the 500-m profiles over a distance of $N_{\mathrm{integ}} \times 500$ m. Translated in the spectral domain, the averaging amounts to multiplying the spectrum $\mathcal{K}$ by a cardinal sine ("sinc"-in-frequency) function. The amplitudes of the sinc filters associated with 1- and 10-km integrations are plotted in Fig. 4 (bottom right). As the integration length increases, the corresponding sinc filter alters the initial shape of $\mathcal{K}$, particularly its tails. Moreover, if the integrated data are downsampled to an $N_{\mathrm{integ}} \times 500$ m spacing, this amounts to truncating the spectrum $\mathcal{K}$ to the frequency range $[-(2N_{\mathrm{integ}}\Delta_{\mathrm{X}})^{-1}, (2N_{\mathrm{integ}}\Delta_{\mathrm{X}})^{-1}]$ km^{-1}. While one expects the random noise to dominate the high-frequency regions of the spectrum, these spectral bands generally contain useful information about the fine spatial features of the atmospheric scene being observed. Instead, by applying a low-pass filter with a smoother decay toward higher frequencies, similar to the filter $\mathcal{L}_{\alpha=3,\beta=2}$ defined in (8) and plotted in Fig. 4 (top right), one has a better chance of identifying the filter that matches the received data [18]. This matched filter increases the SNR of the measured signal while preserving the tails of the spectrum and the potential information therein.

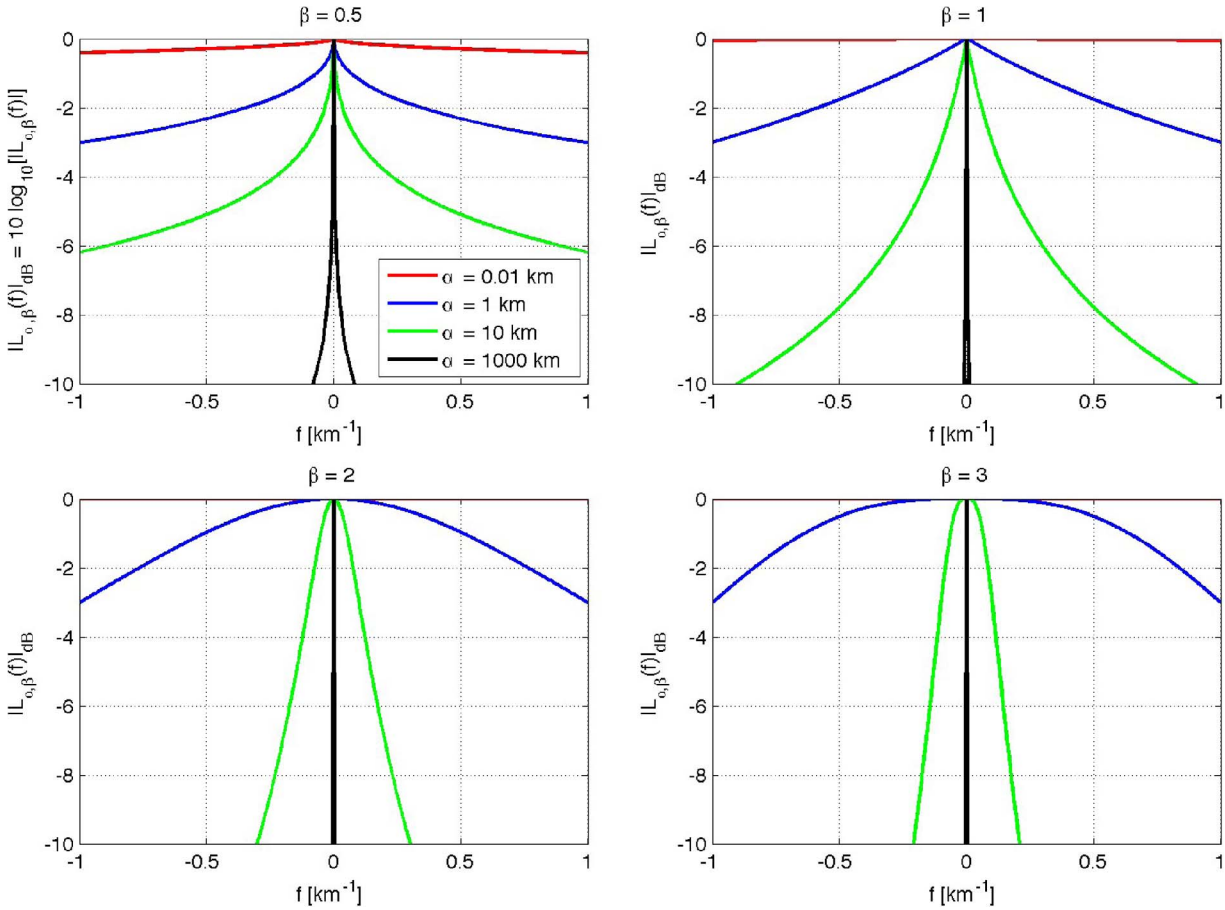

Fig. 5. Examples of filters $\mathcal{L}_{\alpha,\beta}$ for $\alpha \in \{10^{-2}, 1, 10, 10^3\}$ km and $\beta \in \{0.5, 1, 2, 3\}$.

B. Filtering Process

As an alternative to the traditional integration, we propose to apply an adaptive low-pass filter to $\mathcal{K}$ that matches better the spectral signature of the desired signal. The transfer function $\mathcal{L}_{\alpha,\beta}$ of the filter is defined as

$$\mathcal{L}_{\alpha,\beta}(f) = \frac{1}{1+|\alpha f|^{\beta}} \quad \forall\, f \in \mathbb{R} \tag{8}$$

where $\alpha \in \mathcal{A}$ and $\beta \in \mathcal{B}$, with $\mathcal{A}$ and $\mathcal{B}$ given subdomains of $(0, \infty)$. Although $\mathcal{L}_{\alpha,\beta}$ is symmetrical with respect to $f = 0$ km^{-1}, its general expression covers a broad range of filter shapes, as illustrated in Fig. 5.

Increasing the filter constant α narrows the bandwidth of the filters, as can be seen by comparing $\mathcal{L}_{0.01,0.5}$ and $\mathcal{L}_{10,0.5}$. On the other hand, increasing the order β steepens the slopes of the filter, as demonstrated by $\mathcal{L}_{10,0.5}$ and $\mathcal{L}_{10,3}$. However, unlike a truncation, these filters preserve the tails of the spectrum while enhancing the low-frequency portion of the spectrum, as can be seen for $(\alpha = 3, \beta = 2)$ in Fig. 4.

The filtered spectrum $\mathcal{K}_{\alpha,\beta}$ and its inverse Fourier transform $K_{\alpha,\beta}$ are then expressed as

$$\mathcal{K}_{\alpha,\beta}(f, h_{\mathrm{E}}) = \mathcal{L}_{\alpha,\beta}(f)\mathcal{K}(f, h_{\mathrm{E}}) \tag{9}$$

$$K_{\alpha,\beta}(x_{\mathrm{E}}, h_{\mathrm{E}}) = \frac{1}{2\pi}\int_{\mathbb{R}} e^{j2\pi f x_{\mathrm{E}}}\mathcal{K}_{\alpha,\beta}(f, h_{\mathrm{E}})df. \tag{10}$$

Finally, the filtered mean Doppler velocity $\mu_{\alpha,\beta}$ is obtained through PP processing of $K_{\alpha,\beta}$, i.e.,

$$\mu_{\alpha,\beta}(x_{\mathrm{E}}, h_{\mathrm{E}}) = V_{\mathrm{Nyq}}\frac{\arg\left[K_{\alpha,\beta}(x_{\mathrm{E}}, h_{\mathrm{E}})\right]}{\pi}. \tag{11}$$

The general steps described here to compute the filtered velocity $\mu_{\alpha,\beta}$ are schematically summarized in Fig. 6, where they constitute the so-called "Process 1."

C. Optimal Filter Selection

The difficulty in the selection of the optimal filter is to identify the value of (α, β) in $\mathcal{A} \times \mathcal{B}$ that produces the most accurate $\mu_{\alpha,\beta}$, with respect to the reference μ_{TRUE} that is generally unknown. To begin with, in Section IV-C1, we assume the knowledge of μ_{TRUE} and derive an optimal filter that demonstrates the best performance achievable through the filtering approach. In Section IV-C2, we propose an unconstrained optimization criterion that is based *only* on the available observables. Finally, in Section IV-C3, a filter based on constrained optimization is introduced.

1) Error-Based Optimization: In the hypothetical scenario where the reference velocity μ_{TRUE} is available, the *velocity error* $\varepsilon_{\alpha,\beta} = \mu_{\alpha,\beta} - \mu_{\mathrm{TRUE}}$ can be computed. This error will partly consist of aliasing effects affecting the PP estimation

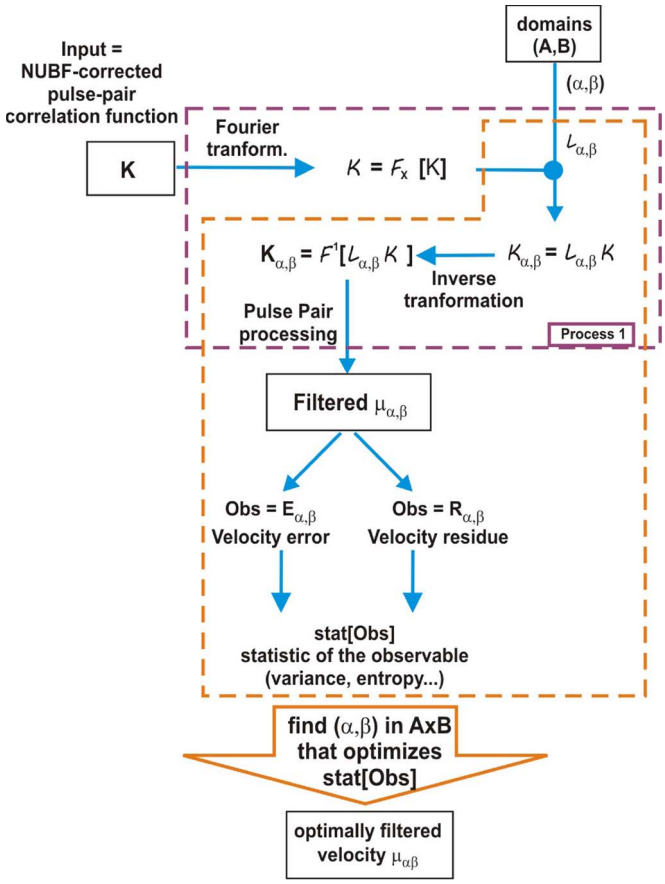

Fig. 6. Summary of the filtering approach: Process 1 describes the evaluation of the filtered velocity $\mu_{\alpha,\beta}$, whereas the rest of the diagram shows the optimization of statistics of the velocity error $E_{\alpha,\beta}$ or residue $R_{\alpha,\beta}$.

of $\mu_{\alpha,\beta}$. To focus on the aliasing-free component of $\varepsilon_{\alpha,\beta}$, the velocity error is defined as

$$E_{\alpha,\beta} = \mu_{\alpha,\beta} - \mu_{\mathrm{TRUE}} \mod (2V_{\mathrm{Nyq}}) = \frac{V_{\mathrm{Nyq}}}{\pi} \arg\left[\exp\left(j\pi \frac{\mu_{\alpha,\beta} - \mu_{\mathrm{TRUE}}}{V_{\mathrm{Nyq}}}\right)\right] \quad (12)$$

where $\mathrm{mod}(\cdot)$ denotes the modulo operator. The optimal filter can be then sought by determining the value of (α, β) that minimizes the RMS error $\sigma[E_{\alpha,\beta}] = \sqrt{\mathbb{E}[E_{\alpha,\beta}^2] - |\mathbb{E}[E_{\alpha,\beta}]|^2}$. The expectation operator $\mathbb{E}[\cdot]$ is defined as

$$\mathbb{E}[E_{\alpha,\beta}] = \frac{1}{N_{\mathrm{pixels}}} \sum_{k=1}^{N_{\mathrm{pixels}}} E_{\alpha,\beta}(x_k, h_k) \quad (13)$$

with N_{pixels} the number of pixels from the scene that are used to compute the statistics. For instance, with a data set comprising N_{X} vertical profiles and N_{H} range bins, if all points are used, then $N_{\mathrm{pixels}} = N_{\mathrm{X}} N_{\mathrm{H}}$. Otherwise, if, e.g., only the points where the SNR is larger than a threshold SNR_0 are used, then $N_{\mathrm{pixels}} \leq N_{\mathrm{X}} N_{\mathrm{H}}$.

Thus, the optimal *"error variance minimizing" (EVM) filter* is characterized by

$$(\alpha_{\mathrm{EVM}}, \beta_{\mathrm{EVM}}) = \underset{(\alpha,\beta)\in\mathcal{A}\times\mathcal{B}}{\arg\min}\ \sigma^2[E_{\alpha,\beta}]. \quad (14)$$

2) Unconstrained Residue-Based Optimization—Maximum Entropy Filter: While the EVM filter is optimal in terms of RMS error reduction, it cannot be obtained in general due to the unavailability of μ_{TRUE}. On the contrary, the *velocity residue* $R_{\alpha,\beta}$ of the filter is a variable that can be computed in practice given its definition as

$$R_{\alpha,\beta} = \mu_{\mathrm{PP}} - \mu_{\alpha,\beta} \mod (2V_{\mathrm{Nyq}}). \quad (15)$$

Similarly to (12), this definition circumvents potential aliasing errors. The objective is to identify statistical measures of $R_{\alpha,\beta}$, the optimization of which is consistent with a minimization of $\sigma^2[E_{\alpha,\beta}]$.

First, an unconstrained filter is developed according to the heuristic argument that the true radar signal μ_{TRUE} is spatially organized by the morphology of the physical atmospheric process that is being observed, whereas the random velocity noise should be a "disorganized" stochastic signal. Hence, when filtering μ_{PP}, if the filter eliminates some meaningful features from the velocity field, these organized features will appear in $R_{\alpha,\beta}$ and therefore reduce the level of disorganization of $R_{\alpha,\beta}$. This rationale can be formalized by quantifying the level of organization of $R_{\alpha,\beta}$ through Shannon's entropy, which is defined as

$$S[R_{\alpha,\beta}] = -\int_{[-V_{\mathrm{Nyq}}, V_{\mathrm{Nyq}}]} f_{R_{\alpha,\beta}}(r) \ln\left[f_{R_{\alpha,\beta}}(r)\right] dr \quad (16)$$

where $f_{R_{\alpha,\beta}}$ is the probability density function (pdf) of $R_{\alpha,\beta}$ obtained by sorting the samples of $R_{\alpha,\beta}$ [19]. Thus, the optimal filter is sought as the one that produces the "least organized" residue, i.e., as a *"residue entropy maximizing" (REM) filter* characterized by

$$(\alpha_{\mathrm{REM}}, \beta_{\mathrm{REM}}) = \underset{(\alpha,\beta)\in\mathcal{A}\times\mathcal{B}}{\arg\min}\ S[R_{\alpha,\beta}]. \quad (17)$$

Compared with the EVM filter, the REM filter may be suboptimal in terms of RMS error reduction. Indeed, given the choices made in the filtering, e.g., the use of the same filter for all range bins, situations can arise where the RMS error reduction is only feasible at the expense of losing some organized spatial features from the radar data, which, once in the velocity residue, will reduce the value of the entropy. However, as a corollary, the REM filter should be very efficient at preserving the morphology of the velocity field.

3) Constrained Residue-Based Optimization—Minimum Variance Filter: The RMS error $\sigma^2[E_{\alpha,\beta}]$ cannot be minimized by optimizing $\sigma^2[R_{\alpha,\beta}]$ without constraints. This can be seen by expressing $R_{\alpha,\beta}$ as a function of $E_{\alpha,\beta}$ and the prefiltering velocity error $E_{\mathrm{PRE}} = \mu_{\mathrm{PP}} - \mu_{\mathrm{TRUE}}$ as follows:

$$R_{\alpha,\beta} = E_{\mathrm{PRE}} - E_{\alpha,\beta} \mod (2V_{\mathrm{Nyq}}). \quad (18)$$

Thus, the variance of $R_{\alpha,\beta}$ reads

$$\sigma^2[R_{\alpha,\beta}] = \sigma^2[E_{\mathrm{PRE}}] + \sigma^2[E_{\alpha,\beta}] - 2\,\mathrm{Cov}[E_{\mathrm{PRE}} E_{\alpha,\beta}] \quad (19)$$

where $\mathrm{Cov}[E_{\mathrm{PRE}} E_{\alpha,\beta}] = \mathbb{E}[E_{\mathrm{PRE}} E_{\alpha,\beta}] - \mathbb{E}[E_{\mathrm{PRE}}]\mathbb{E}[E_{\alpha,\beta}]$. In the right-hand side of (19), $\sigma^2[E_{\mathrm{PRE}}]$ is the variance of the prefiltering-velocity error and is therefore independent from (α, β). The difficulties stem from the term $\mathrm{Cov}[E_{\mathrm{PRE}} E_{\alpha,\beta}]$ as

it involves the filtered velocity error, which depends on (α, β). Hence, it is not easy to relate a minimum of $\sigma^2[E_{\alpha,\beta}]$ to a minimum or a maximum of $\sigma^2[R_{\alpha,\beta}]$, unless $\mathrm{Cov}[E_{\mathrm{PRE}}E_{\alpha,\beta}]$ vanishes. This occurs when 1) the filtering is perfect, i.e., $|E_{\alpha,\beta}| \sim 0$ m $\cdot$ s^{-1}, which is a very optimistic assumption to make *a priori* about the performance of the filter, or when 2) E_{PRE} and $E_{\alpha,\beta}$ are mutually statistically uncorrelated or independent, which is not necessarily true for every (α, β) and therefore amounts to constraining the optimization algorithm.

To eliminate the statistical coupling between $E_{\alpha,\beta}$ and E_{PRE}, one can restrict the domains $\mathcal{A}$ and $\mathcal{B}$ of α and β to the subset $\mathcal{I} \subset \mathcal{A} \times \mathcal{B}$ that leads to a $E_{\alpha,\beta}$ that is *statistically independent* from E_{PRE}. Hence, for any $(\alpha, \beta) \in \mathcal{I}$

$$\sigma^2[R_{\alpha,\beta}] = \sigma^2[E_{\mathrm{PRE}}] + \sigma^2[E_{\alpha,\beta}] \tag{20}$$

and minimizing $\sigma^2[R_{\alpha,\beta}]$ is equivalent to minimizing $\sigma^2[E_{\alpha,\beta}]$. Therefore, the optimal *"constrained residue variance minimizing filter"* (RV) is obtained by solving

$$(\alpha_{\mathrm{RV}}, \beta_{\mathrm{RV}}) = \underset{(\alpha,\beta)\in\mathcal{I}}{\arg\min}\, \sigma^2[R_{\alpha,\beta}]. \tag{21}$$

The requirement of statistical independence between E_{PRE} and $E_{\alpha,\beta}$ is of course stronger than a requirement of uncorrelatedness as it excludes filters, which lead to $E_{\alpha,\beta}$ and E_{PRE} that are statistically dependent despite being uncorrelated. It is worth noting that, once the search space $\mathcal{I}$ has been determined, one can also seek the optimal filter by maximizing the entropy of $R_{\alpha,\beta}$. As shown in Appendix C, this type of filter produces similar results as the RV filters.

a) Optimal search space $\mathcal{I}$: For any $(\alpha, \beta) \in \mathcal{I}$, owing to (18) and the independence between $E_{\alpha,\beta}$ and E_{PRE}, the pdf of $R_{\alpha,\beta}$ matches an expected shape defined as

$$f_{R_{\alpha,\beta}} = f_{E_{\mathrm{PRE}}} * f_{-E_{\alpha,\beta}} \tag{22}$$

where $f_{E_{\mathrm{PRE}}}$ and $f_{-E_{\alpha,\beta}}$ are the pdfs of E_{PRE} and $-E_{\alpha,\beta}$, respectively, whereas the asterisk stands for the convolution. The estimates $\widehat{f}_{E_{\mathrm{PRE}}}$ and $\widehat{f}_{-E_{\alpha,\beta}}$ of $f_{E_{\mathrm{PRE}}}$ and $f_{-E_{\alpha,\beta}}$ are computed following a method that is detailed in Appendix A and summarized in the next section. Then, $\mathcal{I}$ is determined by finding the values of $(\alpha, \beta) \in \mathcal{A} \times \mathcal{B}$ that have a small Kolmogorov–Smirnov statistic $T(\alpha, \beta)$, i.e.,

$$T(\alpha,\beta) = \sup_{v\in\mathbb{R}} \left| F_{R_{\alpha,\beta}}(v) - \widehat{F}_{E_{\mathrm{PRE}}-E_{\alpha,\beta}}(v) \right| \le T_{\max} \tag{23}$$

where $T_{\max} \ge 0$ is a threshold value, and sup denotes the supremum operator. In this equation, $F_{R_{\alpha,\beta}}$ and $\widehat{F}_{E_{\mathrm{PRE}}-E_{\alpha,\beta}}$ are the cumulative distribution functions (cdfs) of $f_{R_{\alpha,\beta}}$ and $\widehat{f}_{E_{\mathrm{PRE}}} * \widehat{f}_{-E_{\alpha,\beta}}$, respectively. The use of the entire cdf of $R_{\alpha,\beta}$ in (23) leads to a more robust search space $\mathcal{I}$ than by matching only the variance of $R_{\alpha,\beta}$ to a target value as is done in the constrained optimization based on uncorrelatedness (see Appendix D).

b) Expected distributions of the filtered and prefiltering velocity errors $E_{\alpha,\beta}$ and E_{PRE}: Given a filter $\mathcal{L}_{\alpha,\beta}$, the pdf $f_{-E_{\alpha,\beta}}$ is estimated by generating an ensemble of realizations of the random process $E_{\alpha,\beta}$. This is done by simulating sequences of (I, Q) samples that vary according to the statistics predicted by the CPR characteristics and assumed turbulence.

TABLE III
SUMMARY OF OPTIMALITY CRITERIA FOR THE SELECTION OF THE FILTERS

Filter type	Optimization criterion	Acronym	Velocities used		
			μ_{PP}	$\mu_{\alpha,\beta}$	μ_{TRUE}
Unconstrained	Error-variance minimum	EVM	✓	✓	✓
	Residue-entropy maximum	REM	✓	✓	–
Constrained	Residue-variance minimum	RVE	✓	✓	✓
		RVA	✓	✓	–

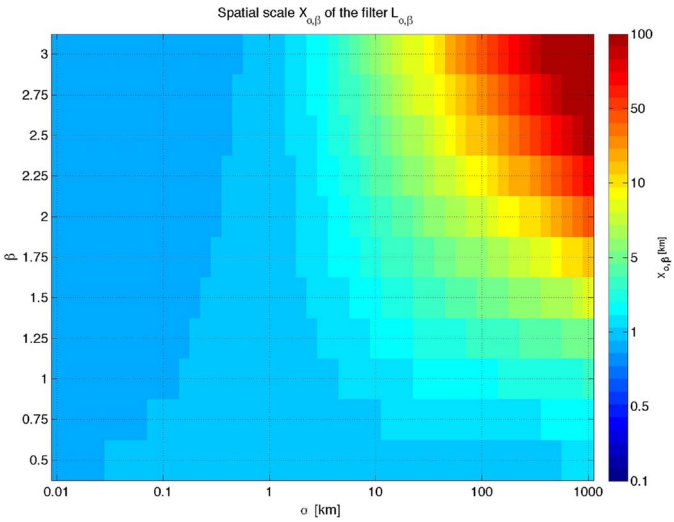

Fig. 7. Spatial scales $X_{\alpha,\beta}$ of the filters for $\alpha \in \mathcal{A} = [10^{-2}, 10^3]$ km and $\beta \in \mathcal{B} = [0.5, 3]$.

As detailed in Appendix A, the simulation of these (I, Q) samples takes into account the SNR distribution in the radar scene of interest and the broadening caused by the spacecraft velocity [11]. The total broadening also includes a $\sim$1 m $\cdot$ s^{-1} contribution from moderate atmospheric turbulence. The obtained voltage samples are then integrated over a distance $X_{\alpha,\beta} = [2\Theta_{\alpha,\beta}]^{-1}$, which represents the scale or characteristic length of the filter, with the noise equivalent bandwidth $\Theta_{\alpha,\beta}$ defined as

$$\Theta_{\alpha,\beta} = \left[\int_{\mathbb{R}} f^2 \mathcal{L}_{\alpha,\beta}(f) df \Big/ \int_{\mathbb{R}} \mathcal{L}_{\alpha,\beta}(f) df \right]^{\frac{1}{2}}. \tag{24}$$

The pdf $f_{E_{\mathrm{PRE}}}$ can be approximated similarly to $f_{-E_{\alpha,\beta}}$, with the only difference that the along-track integration is now performed over 500 m to achieve the level-1B sampling. The resulting approximation of $f_{E_{\mathrm{PRE}}}$ is coined as the *analytical* approximation of $f_{E_{\mathrm{PRE}}}$ and denoted f_{ANA}. The search space obtained using f_{ANA} as an approximation for $f_{E_{\mathrm{PRE}}}$ in (22) and (23) is denoted $\mathcal{I}_{\mathrm{A}}$, and the corresponding optimal filter is written RVA. It is worth noting that f_{ANA} does not account for the presence of residual NUBF velocity errors.

We also consider the filter RVE and its search space $\mathcal{I}_{\mathrm{E}}$ that are obtained using the distribution f_{ERR} of $E_{\mathrm{PRE}} = \mu_{\mathrm{PP}} - \mu_{\mathrm{TRUE}}$, i.e., derived from the measured μ_{PP} and assuming the knowledge of μ_{TRUE}. In general, f_{ERR} will slightly differ from the ideal $f_{E_{\mathrm{PRE}}}$ since f_{ERR} may still be affected by remnants of NUBF errors that could not be removed using the gradient-based correction (6). All the filters described in Section IV-C are listed in Table III.

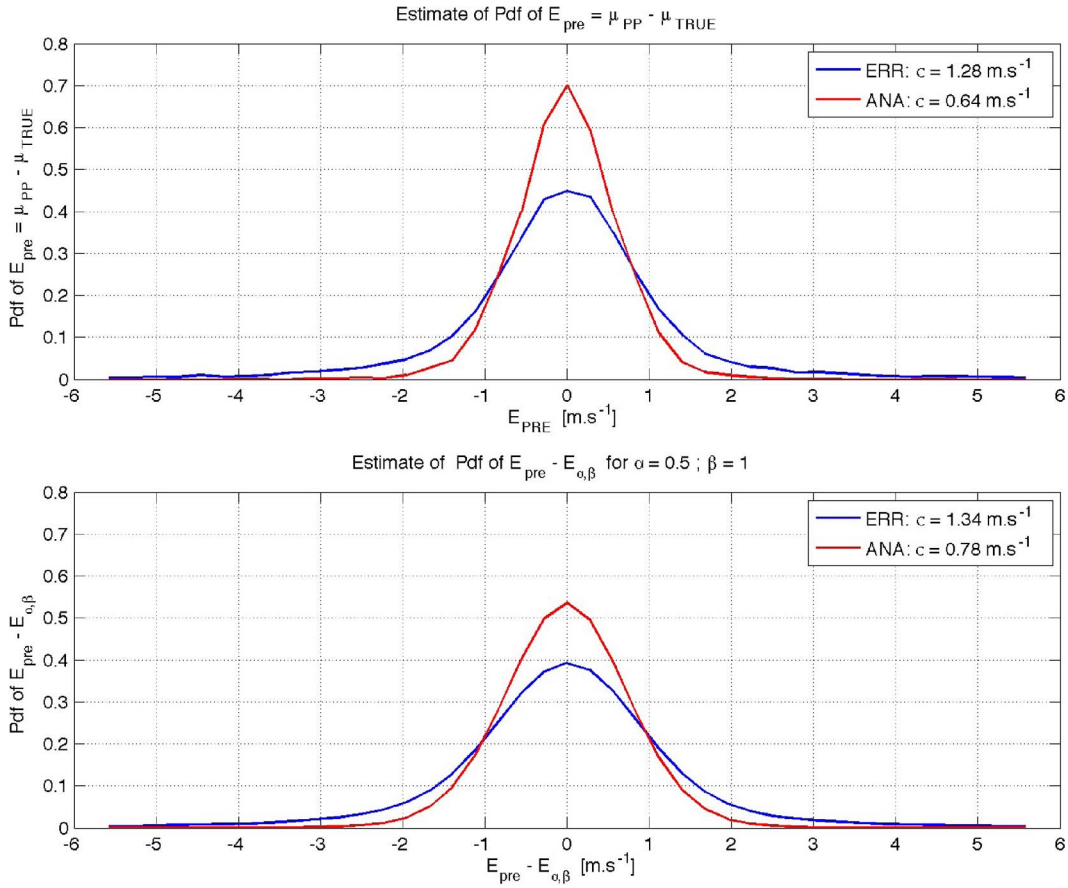

Fig. 8. Snowstorm measured by SPIDER. (Top) pdf of the prefiltering velocity error $f_{E_{\rm PRE}}$ as estimated from the measured error (ERR) or analytically (ANA). (Bottom) Target pdf of the residue obtained by convolving the estimates of $f_{E_{\rm PRE}}$ with $f_{-E_{\alpha,\beta}}$, for $\alpha = 0.5$ km and $\beta = 1$.

V. Results

A. Snowstorm Example

1) Filters: The methods described in Section IV are now applied to the snowstorm case introduced in Section III-A. The bank of filters considered here is obtained by letting α and β vary in the domains $\mathcal{A} = [10^{-2}, 10^{3}]$ km and $\mathcal{B} = [0.5, 3]$. Fig. 5 showed how these ranges cover most of the filter shapes of interest while allowing for a smooth variation of the filter shapes as a function of (α, β). The spatial scales $X_{\alpha,\beta}$ of the filters are plotted in Fig. 7.

Low-order filters $(\beta < 1)$ all have similar scales, i.e., $\sim$1 km, and the values of (α, β) mainly command the smoothness of the decay of the filters at larger frequencies. For higher orders, i.e., $\beta \geq 2$, varying α leads to a transition from "all-pass" filters when $\alpha \leq 0.5$ km (top left corner), which basically leave the velocity unfiltered, to "all-cut" filters when $\alpha \geq 100$ km (top right corner), which perform a moving average over a very long baseline.

The pdf $f_{\rm ERR}$ of the prefiltering velocity error is plotted in Fig. 8 together with the analytical approximation $f_{\rm ANA}$. The analytical estimate produces a narrower distribution ($\sigma_{\rm ANA} = 0.64\ {\rm m \cdot s^{-1}}$) than $f_{\rm ERR}(\sigma_{\rm ERR} = 1.28\ {\rm m \cdot s^{-1}})$ because it does not account for residual NUBF errors. In fact, when the Doppler data are simulated without adding the NUBF effect but with the EC-CPR spectral broadening, the analytical distribution matches the actual prefiltering error distribution. The convolution of these estimates of $f_{E_{\rm PRE}}$ with the distribution of the filtered velocity error $f_{-E_{\alpha,\beta}}$ smears the final distributions $f_{\rm ERR} * f_{-E_{\alpha,\beta}}$ and $f_{\rm ANA} * f_{-E_{\alpha,\beta}}$, as demonstrated by Fig. 8.

2) Filtered Velocities: The statistics of the filtered velocity error and residue are computed over the set of points located above the surface and such that SNR ≥ 6 (i.e., for reflectivities larger than $-21.5 + 6 = -15.5$ dBZ). The limit value of SNR $= 6$ is a suitable choice between the region of high SNR, where little dependence of the Doppler statistics on SNR is observed, and the region of low SNR, where the results strongly depend on the SNR [10]. The evolutions of these statistics, as a function of α and β, are displayed in Fig. 9. For every type of optimization method, the optimal filter is indicated by a star $(\star)$. For the constrained optimizations RVE and RVA (bottom row), the contours of the search spaces $\mathcal{I}_{\rm E}$ and $\mathcal{I}_{\rm A}$ are indicated by dashed lines, for various values of the threshold $T_{\max}$ used in (23), viz., $T_{\max} \in \{0.02, 0.04, 0.06\}$.

The graph of $\sigma[E_{\alpha,\beta}]$ (top left) identifies a region around ($\alpha_{\rm EVM} = 3.2$ km, $\beta_{\rm EVM} = 1.75$) as the set of filters that lead to the smallest RMS error. The optimal EVM filter has a scale $X_{\rm EVM} = 1.2$ km and yields accuracy of $\sigma[E_{\alpha_{\rm EVM},\beta_{\rm EVM}}] = 0.53\ {\rm m \cdot s^{-1}}$. The entropy of the residue (top right) reaches its maximum for ($\alpha_{\rm REM} = 1.3$ km, $\beta_{\rm REM} = 2.75$). The conservative nature of the REM filter in terms of integration length, which is discussed in Section IV-C2, transpires through its scale $X_{\rm REM} = 1.0$ km $< X_{\rm EVM}$ and the corresponding RMS error $\sigma[E_{\alpha_{\rm REM},\beta_{\rm REM}}] = 0.87\ {\rm m \cdot s^{-1}}$ that is larger than the optimum $\sigma[E_{\alpha_{\rm EVM},\beta_{\rm EVM}}] = 0.53\ {\rm m \cdot s^{-1}}$. This general behavior is

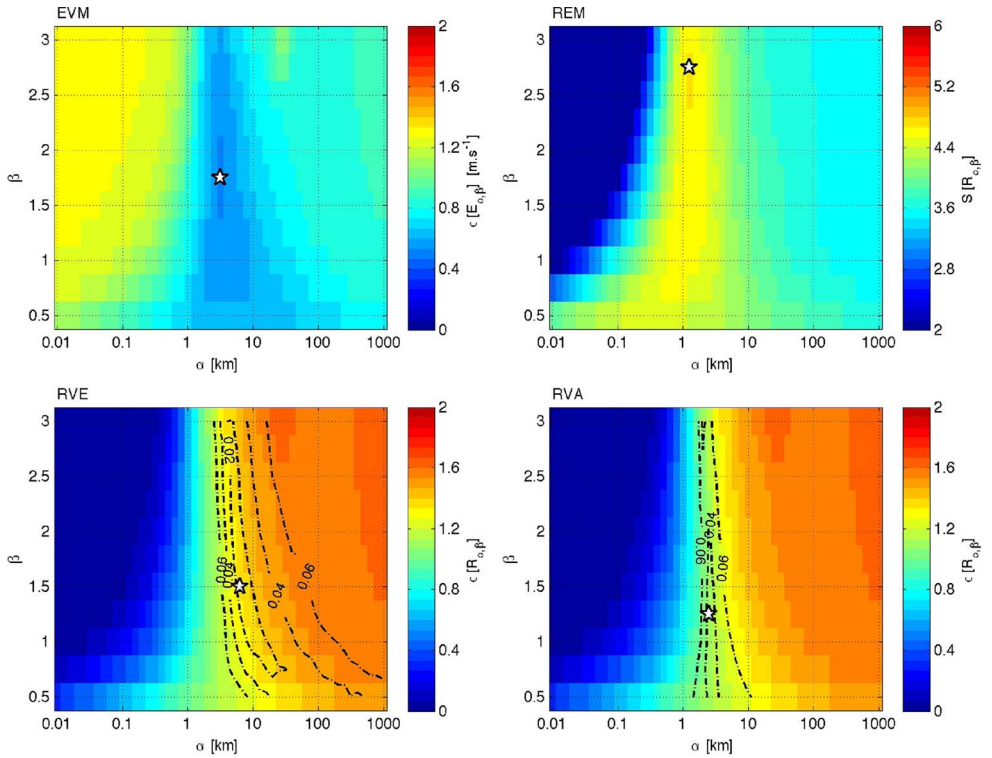

Fig. 9. Snowstorm measured by SPIDER: statistics of the filtered velocity error $E_{\alpha,\beta}$ and residue $R_{\alpha,\beta}$ as a function of (α, β). Unconstrained filters: (top left) EVM filter on the map of $\sigma[E_{\alpha,\beta}]$; (top right) REM filter on the map of $S[R_{\alpha,\beta}]$. Constrained filters: (bottom left) RVE filter and contours of $\mathcal{I}_{\mathrm{E}}$ on the map of $\sigma[R_{\alpha,\beta}]$; (bottom right) RVA filter and contours of $\mathcal{I}_{\mathrm{A}}$ on the map of $\sigma[R_{\alpha,\beta}]$. The filters on the left (EVM and RVE) assume the knowledge of μ_{TRUE}, unlike the filters on the right (REM and RVA).

observed in all our EC-CPR simulations, as will be shown in Section V-B.

The map of $\sigma[R_{\alpha,\beta}]$ (bottom) illustrates why constraints are required to determine the optimal RV filters: an unconstrained minimization of $\sigma[R_{\alpha,\beta}]$ would lead to an all-pass filter (top left corner of $\mathcal{A} \times \mathcal{B}$), whereas an unconstrained maximization of $\sigma[R_{\alpha,\beta}]$ would lead to an all-cut filter (top right corner of $\mathcal{A} \times \mathcal{B}$). The search spaces $\mathcal{I}_{\mathrm{E}}$ and $\mathcal{I}_{\mathrm{A}}$ of the RVE and RVA methods both correspond to areas where $\sigma[E_{\alpha,\beta}]$ is also small. This allows being confident about the rationale proposed to constrain the optimization of the variance of the residue. Moreover, the iso-$T_{\max}$ contours on the map of $\sigma[R_{\alpha,\beta}]$ show that $\mathcal{I}_{\mathrm{E}}$ can be determined even by using a threshold as small as $T_{\max} = 0.02$ in (23), i.e., allowing a maximum discrepancy of 2% between the cdf of $R_{\alpha,\beta}$ and the target cdf $\widehat{F}_{E_{\mathrm{PRE}}-E_{\alpha,\beta}}$. This threshold $T_{\max} = 0.02$ would, however, be too selective to identify $\mathcal{I}_{\mathrm{A}}$, which requires $T_{\max} \geq 0.04$. This smallest usable value of $T_{\max}$ represents the error budget that one needs to tolerate in the test of (23) to account for the fact that f_{ANA} does not include the effect of residual NUBF errors, as discussed in Section V-A1. However, with a $T_{\max}$ that is too large, the corresponding set $\mathcal{I}$ would contain filters that no longer comply with the criterion of statistical independence enunciated in (22). In our simulations, we have used $T_{\max} = 0.05$.

More than the dependence of the statistics of $E_{\alpha,\beta}$ and $R_{\alpha,\beta}$ on (α, β), the bottom-line indicators of the performance of the filter are the RMS error and the morphology of the filtered velocity. The performance of the various filters is summarized in Table IV, which lists the final RMS error of the filtered velocity together with an efficiency coefficient. This coefficient, which is denoted

TABLE IV
PERFORMANCE OF THE OPTIMAL FILTERS (SPATIAL SCALE $X_{\alpha,\beta}$, RMS ERROR σ, AND EFFICIENCY η) FOR THE SPIDER SNOWSTORM EXAMPLE

Filter type	Filter scale $X_{\alpha,\beta}$ [km]	rms error σ [$\mathrm{m \cdot s^{-1}}$]	efficiency η [%]
Pre-filtering	-	1.27	-
EVM	1.2	0.53	100
REM	1.0	0.87	64
RVE	1.4	0.58	96
RVA	1.1	0.55	98
1 km integration	1.0	0.89	62
5 km integration	5.0	0.94	55
10 km integration	10.0	0.96	52

η, compares the error reduction achieved by any of the filters to the ideal error reduction achieved by the EVM filter. For instance, the efficiency $\eta(\mathrm{REM})$ of the REM filter is given by

$$\eta(\mathrm{REM}) = \frac{\sigma^2_{\mathrm{PRE}} - \sigma^2\left[E_{\alpha_{\mathrm{REM}},\beta_{\mathrm{REM}}}\right]}{\sigma^2_{\mathrm{PRE}} - \sigma^2\left[E_{\alpha_{\mathrm{EVM}},\beta_{\mathrm{EVM}}}\right]}. \tag{25}$$

The sign of η is positive if the filter improves the accuracy of the velocity and vice versa. To put these numbers in perspective, we also compute the efficiency of the standard along-track integration methods discussed in Section III-A.

All the filters have spatial scales on the order of $X_{\alpha,\beta} \sim 1$ km and lead to a bigger improvement in accuracy than a standard 1-km along-track integration. The RVE and RVA filters produce error reductions similar to the ideal EVM filter. The high performance of the RVA approach may appear surprising when

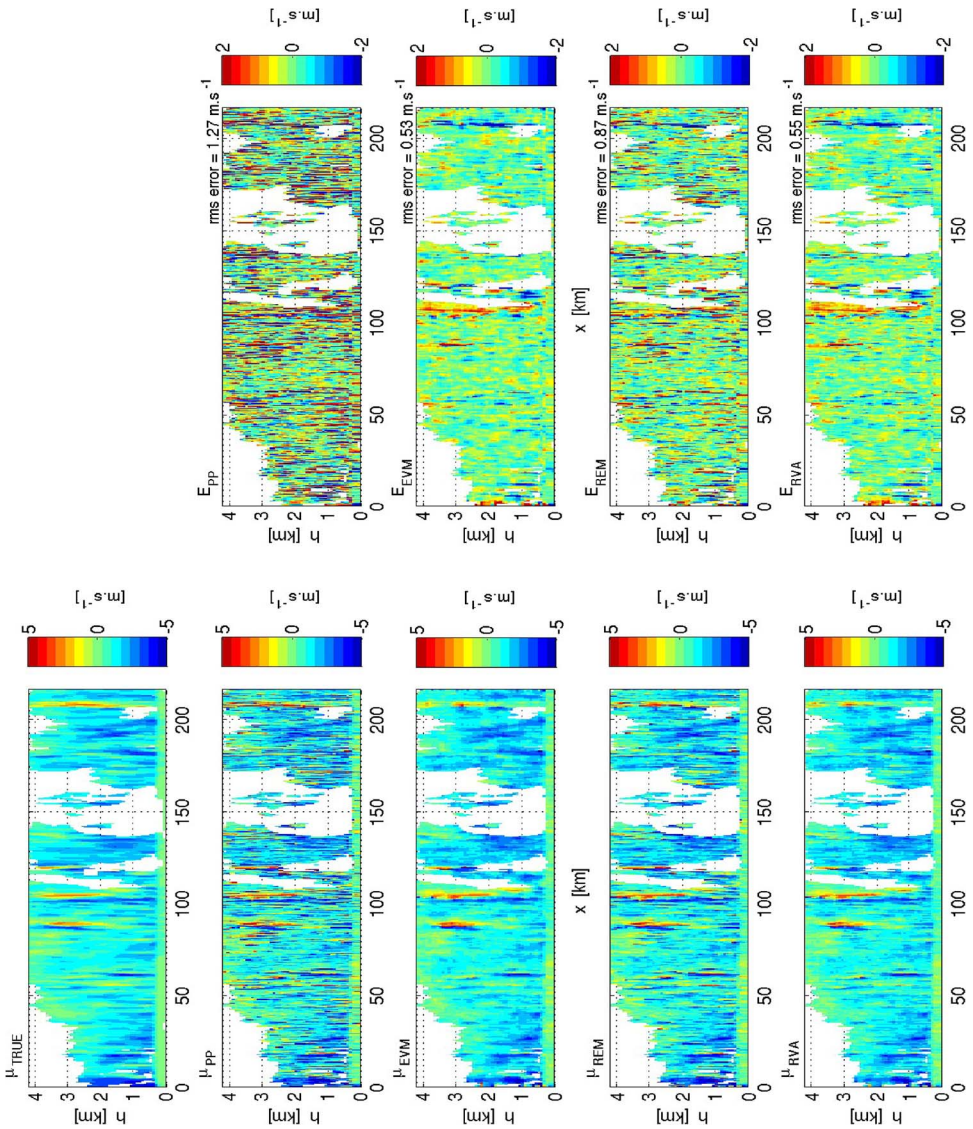

Fig. 10. (Left) Mean Doppler velocity estimate and (right) associated error with respect to μ_{TRUE}: (top row) reference velocity μ_{TRUE}, (second row) prefiltering velocity μ_{PP}, optimally filtered velocity according to (third row) EVM, (fourth row) REM, (bottom row) RVA logics.

considering that it leads to even better results than the RVE approach, which uses f_{ERR}. However, unlike f_{ERR}, which can be affected by residual NUBF errors, the construction of f_{ANA} is entirely based on the random noise, making it a more representative distribution of the statistics of the error one should achieve if all corrections succeed.

To qualitatively illustrate the effects of the filters, the 2-D curtain sections of the optimally filtered velocities are plotted in Fig. 10 together with their error with respect to μ_{TRUE}. These graphs highlight the general improvement both in terms of clarity of the images and of accuracy, particularly when compared with the prefiltering data. Although the EVM filter leads to the smallest RMS error, the map of the filtered-velocity error (3rd row right) shows that it eliminates some organized features, e.g., around $x \in [100, 120]$ km. On the contrary, despite its higher RMS error, the REM-filtered velocity (4th row right) preserves those features, as expected from the maximum-entropy principle at the core of the REM approach.

3) Retrieval of the Mean Velocity CFAD: Contour frequency by altitude diagrams (CFAD) offers a statistical representation of the vertical distribution of the velocity within a regime or a scene of interest. For instance, the CFAD of μ_{TRUE} is shown in Fig. 11 (top left) together with the CFADs of the PP velocities integrated along track over 500 m (level-1B) and 1, 5, and 10 km, which are denoted $\mu_{\mathrm{PP}}(500\ \mathrm{m})$, $\mu_{\mathrm{PP}}(1\ \mathrm{km})$, $\mu_{\mathrm{PP}}(5\ \mathrm{km})$, and $\mu_{\mathrm{PP}}(10\ \mathrm{km})$, respectively. The main features of the CFAD of μ_{TRUE} are summarized in the 5%, 50%, and 95% quantiles (top right), which are denoted q_5, q_{50}, and q_{95}, respectively. The differences between the CFAD of μ_{TRUE} and the CFADs of the PP velocities are quantified through the errors of the quantiles, which are also plotted (second to fifth rows, right).

The CFAD of the true velocity shows that μ_{TRUE} is in the range $[-4, 4]\ \mathrm{m \cdot s^{-1}}$. As expected from a precipitating event, the median velocity is negative, viz., between -2 and $-0.8\ \mathrm{m \cdot s^{-1}}$. The localized convective regions, which can be seen in Fig. 10 above $h \sim 2$ km, appears in the CFAD as the small set of points identified by the dashed box.

When considering the PP velocities, the general trend of the distribution of μ_{TRUE}, assessed by q_{50}, remains stable even in $\mu_{\mathrm{PP}}(500\ \mathrm{m})$. This is consistent with the nature of the

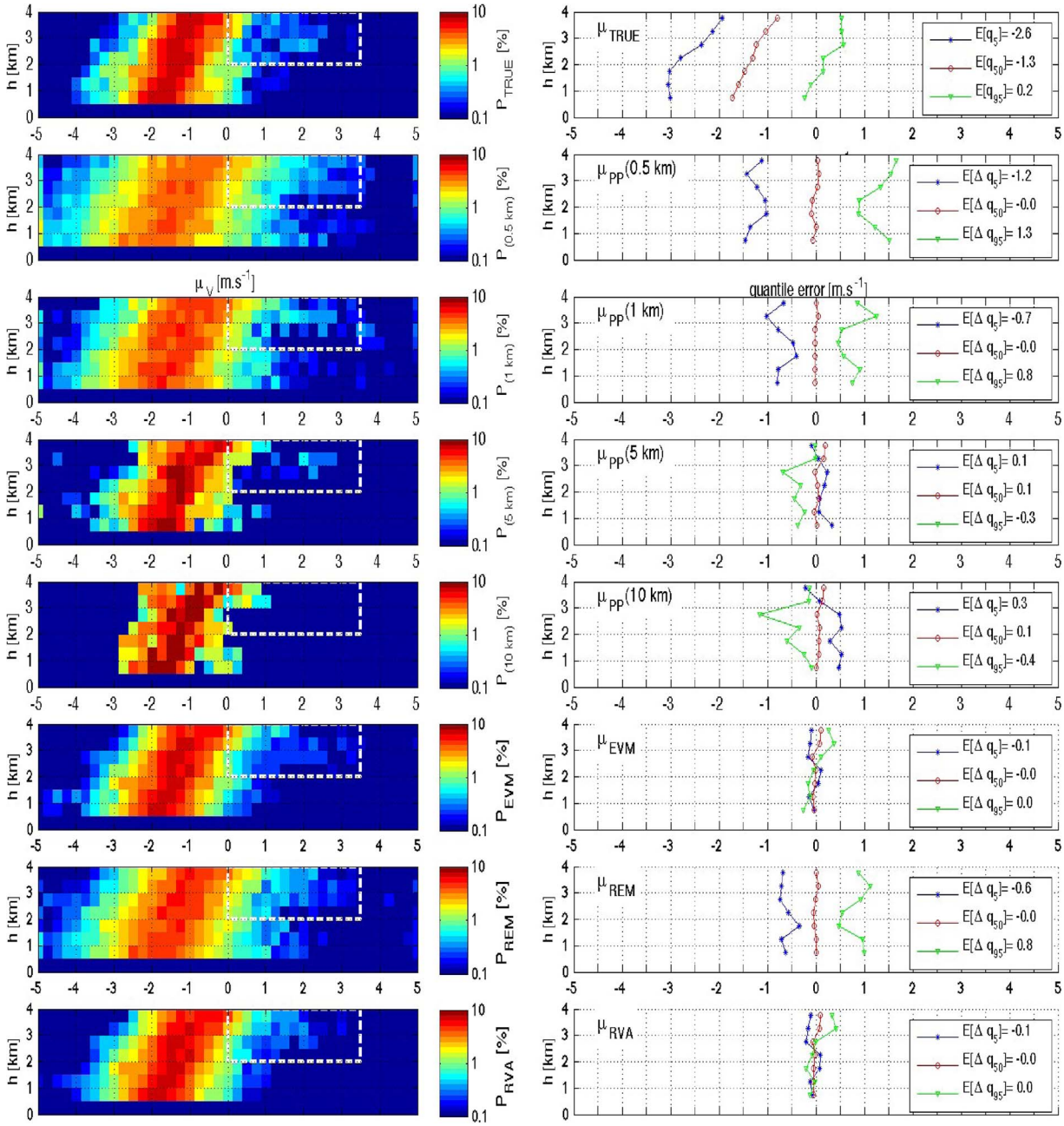

Fig. 11. Effect of the longer along-track integration and adaptive filtering on the distribution of the mean Doppler velocity: (top row) true mean velocity μ_{TRUE}, PP velocity μ_{PP} integrated along track over (second row) 500 m, (third row) 1 km, (fourth row) 5 km, and (fifth row) 10 km and velocities filtered according to (sixth row) EVM, (seventh row) REM, and (bottom row) RVA logics. (Left column) CFAD, (top right) quantiles of μ_{TRUE} and (second to seventh row, right) quantile errors of the integrated μ_{PP}.

velocity noise, which does not introduce any systematic bias. However, the noise causes the dynamic range of $\mu_{\mathrm{PP}}(500\ \mathrm{m})$ to exceed the range of μ_{TRUE}, which translates in a broadening of the CFAD, i.e., an underestimation of q_5 by $\sim 1.2\ \mathrm{m \cdot s^{-1}}$ and an overestimation of q_{95} by $\sim 1.3\ \mathrm{m \cdot s^{-1}}$. Furthermore, at lower range bins $(h < 2\ \mathrm{km})$, the CFAD of $\mu_{\mathrm{PP}}(500\ \mathrm{m})$ erroneously indicates the presence of large updrafts, which actually correspond to aliased velocities. As the integration length is increased to 1 km, the errors of the upper and lower quantiles drop by 60%; however, the contributions from aliased velocities at lower range bins are still visible. The accuracy of the quantiles significantly improves with $\mu_{\mathrm{PP}}(5\ \mathrm{km})$ and $\mu_{\mathrm{PP}}(10\ \mathrm{km})$. However, the coarse spatial resolution of these products appears in the CFAD where the ranges of $\mu_{\mathrm{PP}}(5\ \mathrm{km})$ and $\mu_{\mathrm{PP}}(10\ \mathrm{km})$ are smaller than the actual range of μ_{TRUE}, as shown by the overestimation (underestimation) of q_5 (q_{95}). This clearly shows that an excessive integration leads to a coarse averaging of the entire scene and, therewith, a loss of information, as visible, for example, in the loss of information inside the dashed box.

Similarly, the CFADs of the various filtered velocities are compared with the CFAD of μ_{TRUE} in Fig. 11. The ideal EVM filter reproduces the true CFAD accurately, as evidenced by the quantile errors that are all smaller than $0.1\ \mathrm{m \cdot s^{-1}}$. Moreover, the filters have an antialiasing effect, as can be seen from the lowest range bins that no longer exhibit excessively large positive

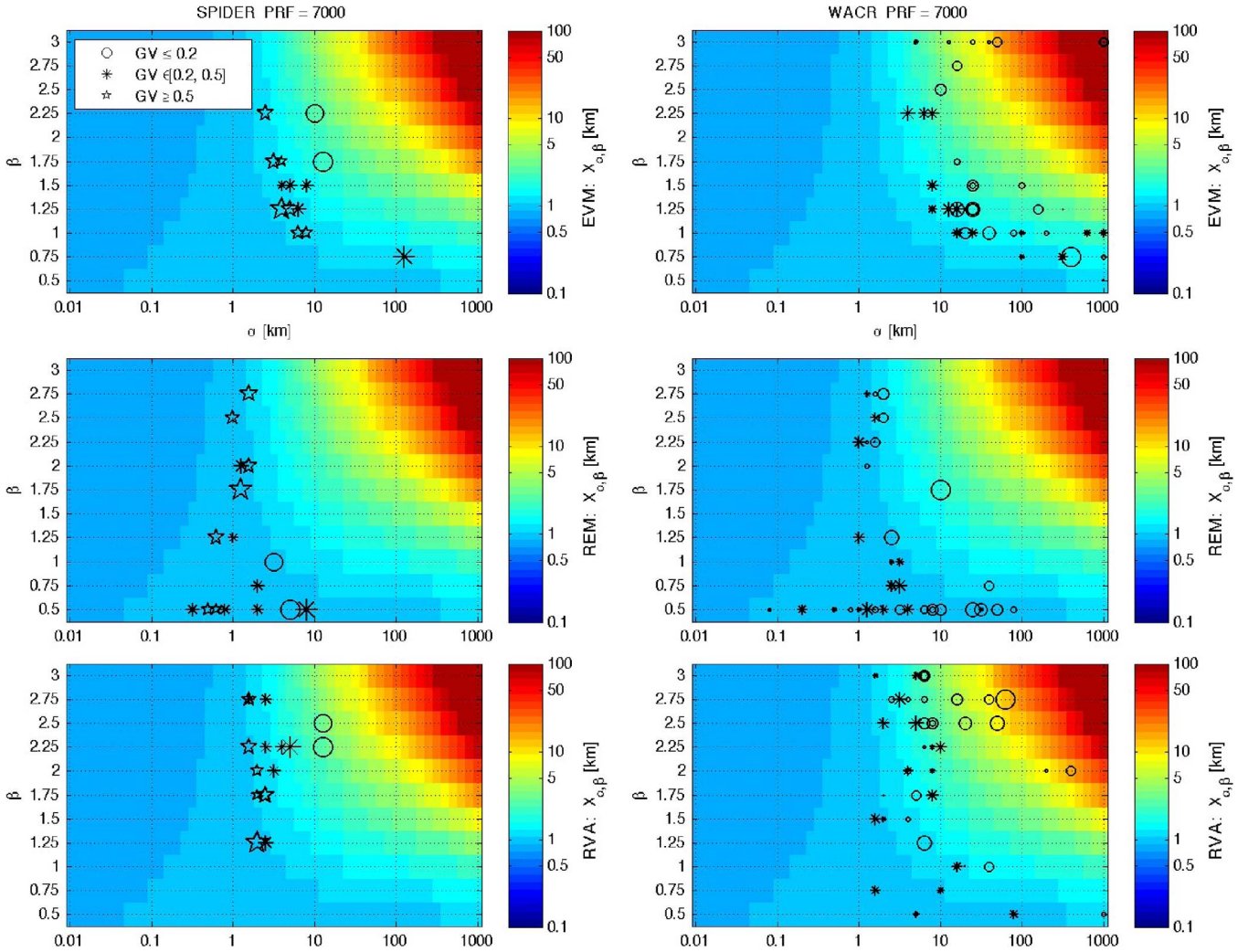

Fig. 12. Distribution of the optimal filters on the map of filter scales $X_{\alpha,\beta}$ for the (left) SPIDER and (right) WACR data sets, at PRF $= 7$ kHz: optimal (top row) EVM, (middle row) REM, and (bottom row) RVA filters. The sizes of the markers are normalized according to the number of pixels per scene. The various markers correspond to the mean values of GV $= \mathbb{E}[|\nabla_x \mu_{\mathrm{TRUE}}|]$ in $[\mathrm{m} \cdot \mathrm{s}^{-1} \cdot \mathrm{km}^{-1}]$.

velocities. A similar performance is achieved with the RVA filter, for which the quantile error is smaller than 0.1 $\mathrm{m} \cdot \mathrm{s}^{-1}$. Although the REM filter does not match the performance of the RVA filter, it still reduces the quantile error to $\sim$0.7 $\mathrm{m} \cdot \mathrm{s}^{-1}$.

B. General Statistics and Discussion

The efficiency of the velocity-filtering approach is now assessed using a larger set of EC-CPR simulations done at PRF values of 6.1, 7, and 7.5 kHz. These simulations are performed starting from high-resolution W-band Doppler measurements obtained from ground-based and airborne radars. Apart from localized occurrences of moderate convection similar to the example of Section V-A, neither data set contains strong convective cases.

The airborne data sets were acquired by NICT's SPIDER radar in January 2003 in Wakasa Bay, Japan. On average, each SPIDER record lasts 23 min. The events recorded mainly consist of precipitation either in the form stratiform rain or snowstorms. The ground-based data sets were obtained between 2006 and 2009, during field campaigns of the W-band Atmospheric Radiation Measurement Program Cloud Radar (WACR) of the U.S. Department of Energy [20]. Every WACR data set represents 24 h of data, which are translated into spatial coordinates using the local advection speed. These measurements cover a larger variety of scenarios, including cirrus and cumulus clouds and tropical and stratiform rain.

The SPIDER and WACR data sets are segmented into records that are all 100 km long in the along-track direction. Hence, all the filters are sampled at the common spectral resolution $\Delta f = 1/100\ \mathrm{km}^{-1}$. On the one hand, this segmentation allows having enough pixels per scene to compute meaningful statistics of the velocity (variance, entropy), which are then used to optimize the filter. On the other hand, this segmentation produces enough test cases (16 SPIDER scenes and 41 WACR scenes) for the evaluation of general statistics of the filtering method. One could also consider a segmentation of the data set based on the modulus of the along-track gradient of the velocity, i.e., $|\nabla_x \mu|$. However, the value of $\nabla_x \mu_{\mathrm{PP}}$ is affected by the noisiness of the measured velocity itself. Even assuming that $|\nabla_x \mu_{\mathrm{TRUE}}|$ could be estimated, the effect of the adaptively changing window size would contaminate the analysis of the filter performance.

1) Distribution of the Optimal Filters: Fig. 12 displays the distribution of the optimal EVM, REM, and RVA filters on the

TABLE V
GENERAL STATISTICS FROM SPIDER- AND WACR-BASED EC-CPR SIMULATIONS

		PRF = 6.1 kHz			PRF = 7 kHz			PRF =7.5 kHz		
	SNR range	[1.5,6]	[6,16.5]	≥ 16.5	[1.5,6]	[6,16.5]	≥ 16.5	[1.5,6]	[6,16.5]	≥ 16.5
SPIDER simulations										
$\sigma(E_u)$ $[\mathrm{m \cdot s^{-1}}]$	$u =$ pre	2.15	1.69	1.49	1.91	1.33	1.04	1.76	1.16	0.88
	$u =$ EVM	0.73	0.54	0.51	0.69	0.45	0.39	0.64	0.41	0.35
	$u =$ REM	1.45	1.17	1.13	0.98	0.69	0.60	0.85	0.57	0.47
	$u =$ RVE	1.01	0.63	0.54	0.87	0.52	0.42	0.95	0.49	0.38
	$u =$ RVA	1.04	0.62	0.55	0.89	0.54	0.44	0.91	0.52	0.42
$\sigma(E_{\mathrm{PP}})$ $[\mathrm{m \cdot s^{-1}}]$ after along-track integration	1 km	1.64	1.18	0.96	1.38	0.88	0.63	1.18	0.73	0.52
	5 km	1.09	0.78	0.77	0.95	0.68	0.72	0.95	0.68	0.71
	10 km	0.97	0.75	0.89	0.93	0.72	0.87	0.89	0.71	0.87
WACR simulations										
$\sigma(E_u)$ $[\mathrm{m \cdot s^{-1}}]$	$u =$ pre	2.03	1.54	1.30	1.70	1.14	0.85	1.52	0.98	0.73
	$u =$ EVM	0.48	0.35	0.33	0.39	0.29	0.28	0.37	0.27	0.26
	$u =$ REM	1.37	0.96	0.91	0.71	0.46	0.44	0.48	0.36	0.35
	$u =$ RVE	0.53	0.39	0.35	0.45	0.37	0.34	0.47	0.38	0.32
	$u =$ RVA	0.63	0.40	0.36	0.57	0.35	0.33	0.61	0.36	0.33
$\sigma(E_{\mathrm{PP}})$ $[\mathrm{m \cdot s^{-1}}]$ after along-track integration	1 km	1.51	1.06	0.84	1.17	0.78	0.58	1.00	0.66	0.49
	5 km	0.97	0.63	0.58	0.76	0.53	0.51	0.72	0.52	0.49
	10 km	0.78	0.59	0.61	0.68	0.53	0.57	0.66	0.54	0.59

map of filter spatial scales $X_{\alpha,\beta}$, at PRF$=7$ kHz. This graph is also representative of the results obtained at PRF$=6.1$ kHz and PRF$=7.5$ kHz. The optimal filters are indicated by different markers depending on the value of GV$=\mathbb{E}[|\nabla_x \mu_{\mathrm{TRUE}}|]$, i.e., the average modulus of the along-track gradient of the reference velocity (stars for GV $\leq 0.2\,\mathrm{m \cdot s^{-1} \cdot km^{-1}}$, asterisks for GV $\in [0.2, 0.5]\,\mathrm{m \cdot s^{-1} \cdot km^{-1}}$ and circles for GV $\geq 0.5\,\mathrm{m \cdot s^{-1} \cdot km^{-1}}$). The variable GV is a bulk indicator of the spatial variability of the velocity field. Furthermore, the sizes of the markers are proportional to the number of pixels present in each scene. This figure shows that the SPIDER simulations comprise cases with higher spatial variability (indicated by the stars) than the WACR data.

The distribution of $(\alpha_{\mathrm{EVM}}, \beta_{\mathrm{EVM}})$ shows that the scale X_{EVM} is mainly driven by the magnitude of the spatial gradients of the Doppler data, i.e., the amount of information contained in the scene: the smaller the value of GV, the larger the scale of the filter, i.e., the longer the along-track averaging performed by the filter. In terms of the EVM markers, this translates into the fact that, generally, the stars are on the left of the asterisks, which, in turn, are on the left of the circles in the $\mathcal{A} \times \mathcal{B}$-plane. It is worth noting that for one of the scenes measured by WACR (top right), the EVM approach leads to an "all-cut" filter, which integrates the scene entirely in the along-track direction. This scene actually corresponds to a 100-km segment of homogeneous cloud with very little along-track variability of the Doppler velocity (as testified by the circle identifying the scene in Fig. 12) and for which one can afford a very long along-track integration. This illustrates the adaptive nature of the filter scale with respect to the along-track variability of the velocity field. Moreover, the diversity of filter orders β_{EVM} shows that there is not necessarily a universal filter that can accommodate all the various measurements. Hence, the adaptive order of the filter captures the variability of the meteorological event recorded by the CPR.

Similar observations can be made about the scales of the RVA filter, which is usable in practice, unlike the EVM filter. As for the REM filter, its scale remains close to $\sim$1 km. Despite this conservative integration scale compared with X_{EVM}, the REM filter still outperforms a standard 1-km along-track integration in terms of improvement of the accuracy of the velocity, as will be shown in the next section. All these results indicate that the scale of the filter is a bulk variable that provides qualitative information about the performance of the filter, but does not capture the full effect of the filter when applied to the measured velocity.

2) Accuracy of the Filtered Velocity: Table V provides the final RMS errors of the various filters for the SPIDER- and WACR-based simulations. For every scene in the SPIDER and WACR data sets, the accuracy of the Doppler velocity is computed for three ranges of SNR, viz., the low-SNR range [1.5,6] (i.e., $Z_{\mathrm{PP}} \in [-20, -16.5]$ dBZ), the mid-SNR range [6, 16.5] (i.e., $Z_{\mathrm{PP}} \in [-16.5, -5]$ dBZ), and the high-SNR range $[16.5, \infty)$ (i.e., $Z_{\mathrm{PP}} \geq -5$ dBZ). The results reported in Table V correspond to the averages of these SNR-binned statistics weighted by the number of pixels present in each data set.

The results in both data sets are consistent, with the errors in the SPIDER simulations being slightly larger (by $\sim 0.2\,\mathrm{m \cdot s^{-1}}$) than in the WACR due to the larger dynamic variations of the SPIDER data. This larger variability also implies a larger impact of NUBF residuals that persist even after applying NUBF corrections.

For the weak signals (SNR ≤ 6), where the intrinsically uncorrelated thermal noise plays an important role, a standard

longer along-track integration reduces the RMS error of the velocity with respect to μ_{TRUE} (sampled at 500-m along-track spacing as in Section III-A). However, as the SNR increases, the advantage of a longer integration beyond 5 km disappears, particularly for SNR ≥ 16.5, where the RMS error is larger after a 10-km integration than after a 5-km integration. These results show the limited gain in accuracy achievable by longer along-track integration. Similar to Section V-A, this is due to the fact that, beyond a certain integration length, most of the dynamics of Doppler signal is lost and leads to a constant RMS error that represents the energy of the true mean velocity lost in the process of integrating.

The results obtained with the ideal EVM filter show the large gains in accuracy potentially achievable via the filtering method across the ranges of PRF and SNR. Even with the practical RVA filter that does not rely on μ_{TRUE}, an accuracy of 0.4–0.5 $\mathrm{m \cdot s^{-1}}$ is achievable at SNR ≥ 6, while preserving the 500-m horizontal sampling and a horizontal resolution of 2 km or better. The high resemblance between RVE and RVA results shows that the RVA filter matches the best performance achievable by using this type of constrained-optimization approach. These encouraging results comfort the postulate that we made about the statistical independence of the prefiltering and ideally filtered velocity to elaborate the constrained-optimization method. The residual NUBF errors have a stronger impact on the performance of the RVA filter at lower SNR values, as can be seen by comparing the SPIDER and WACR RMS errors. Indeed, these smaller SNR values include transition regions between clear-air and clouds and precipitation, i.e., regions that are prone to uncompensated NUBF biases.

Despite its conservative integration length ($\sim$1 km), the entropy-based REM filter improves the accuracy of the velocity more than a traditional 1-km integration, particularly at higher PRF. The improvement at higher PRF partly stems from the fact that more (I, Q) samples are used to compute the level-1B PP velocity (96 more (I, Q) samples at PRF $= 7.5$ kHz than at PRF $= 6.1$ kHz), and these samples have a stronger mutual correlation. Both factors contribute to reducing the effect of the finite radar sampling on the accuracy of the velocity estimate. As a result, the errors in the Doppler velocity are mainly due to the fluctuations caused by the random reshuffling of hydrometeors within the radar resolution volume and thermal noise. This is a type of uncertainty for which the maximum entropy principle of the REM filter is well suited.

The final accuracy of 0.4–0.5 $\mathrm{m \cdot s^{-1}}$ obtained using the matched filters could be improved by resorting to more advanced filters such as height-adaptive or multiresolution filters. However, the largest gains would be obtained by improving the quality of the NUBF corrections. This would only be feasible through a finer along-track sampling of the Doppler data to increase the chance of capturing the subbeam variation of the radar reflectivity within the radar footprint, which causes the NUBF velocity biases.

VI. Conclusion

Here, a method for filtering the random noise that affects spaceborne Doppler measurements of atmospheric velocities has been presented. The proposed method hinges on an adaptive statistical low-pass filter that applies to the PP correlation function of the Doppler data and therefore sidesteps potential aliasing artifacts. The parameters of the filters are found by solving optimization problems formulated in terms of the statistics of the prefiltering and filtered Doppler velocities. This adaptive matched filtering method has been applied to EarthCARE CPR simulations, which do not include strong convective cases.

The optimal performance of the filters were established by assuming the knowledge of the true velocity. These results show that the accuracy of the Doppler velocity, which is $\sim$1.5 $\mathrm{m \cdot s^{-1}}$ ($\sim$0.9 $\mathrm{m \cdot s^{-1}}$) at PRF $= 6.1$ kHz (7.5 kHz) after applying the NUBF corrections, could be improved to as low as $\sim$0.4 $\mathrm{m \cdot s^{-1}}$ in RMS sense, with minor PRF dependence. The practical implementation of the filters does not assume the knowledge of the true velocity and simply uses the measured PP data. These practical filters achieve more than 90% efficiency in terms of reduction of the variance of the velocity error and yield an RMS error of $\sim$0.5 $\mathrm{m \cdot s^{-1}}$, with minor dependence on the PRF of EC-CPR and for SNR ≥ 6. These performances could be further improved by improving the quality of the NUBF corrections that are applied prior to the filtering. Overall, our results indicate that the RVA filters are well suited for cases of uniform beam filling, whereas the REM filters are better for preserving the spatial features of the velocity field and therefore well indicated for scenes with higher spatial variability.

Despite being more computationally involved than a classical along-track integration, the filtering approach produces a larger improvement in the accuracy of the Doppler data both in terms of the RMS error and in terms of the spatial resolution of the data. These gains in the accuracy of the velocity have been shown to help postprocessing tasks such as dealiasing or the retrieval of the vertical distribution of the atmospheric velocity.

This work could potentially revert the paradigm of traditional spaceborne Doppler data filtering, which implies increasing the integration length and sacrificing the horizontal resolution to reduce the random noise of the Doppler data. While a long along-track integration is justifiable in terms of noise reduction when the scene exhibits minimal along-track variability, our results, which typically involve integration scales smaller than 5 km, show that there is a lot to be gained by avoiding excessive along-track integration, viz., longer than 5 km for the cases studied in this paper.

The bank of filters used in this paper are real-valued and involve two degrees of freedom, viz., the constant and the order of the filter. More advanced filters could be considered, either by allowing for more degrees of freedom in the shapes of the filters or by considering complex-valued filters. Moreover, multiresolution filters could be employed to better take into account the spatial variability of the Doppler data. For instance, in an operational context, the spectral resolution of the filters or, equivalently, the along-track length of the scene being analyzed, could be chosen according to the type of scene being observed, estimated using a cloud mask, or the spatial variability of the velocity field, provided that it can be accurately estimated. In all these cases, the same optimization strategy can be employed, i.e., using the variance or the entropy of the residue of the filters.

TABLE VI
LIST OF SYMBOLS

Symbol	Definition
$\boldsymbol{M}_{\rm E}(x_{\rm E}, h_{\rm E})$	Point $\boldsymbol{M}_{\rm E}$ of along-track coordinate $x_{\rm E}$ and range $h_{\rm E}$
$\mathcal{V}(\boldsymbol{M}_{\rm E})$	EC-CPR resolution volume about the point $\boldsymbol{M}_{\rm E}$
$N_{\rm X},\ N_{\rm H}$	Number of EC-CPR profiles and range gates for a given scene
$\Delta_{\rm X},\ \Delta_{\rm H}$	Along-track and range-gate spacing of EC-CPR measurements
$f_{\rm X},\ f_{\rm H}$	Two-way antenna pattern and range-weighting function
$\mathcal{X}, \mathcal{H}$	Supports of $f_{\rm X}$ and $f_{\rm H}$
$P_{\rm IN},\ P_{\rm TRUE},\ P_{\rm E}$	Input and true Doppler spectra, and spectrum as observed by EC-CPR
$(Z_{\rm IN}, \mu_{\rm IN}, \sigma_{\rm IN})$	Moments of $P_{\rm IN}$: reflectivity $Z_{\rm IN}$, mean velocity $\mu_{\rm IN}$ and width $\sigma_{\rm IN}$
$(Z_{\rm TRUE}, \mu_{\rm TRUE})$	Doppler moments of $P_{\rm TRUE}$, taken as the truth
$\nabla_x Z_{\rm TRUE},\ \nabla_x \mu_{\rm TRUE}$	Along-track gradients of $Z_{\rm TRUE}$ and $\mu_{\rm TRUE}$
$\mathrm{GV} = \mathbb{E}[\lvert\nabla_x \mu_{\rm TRUE}\rvert]$	Average magnitude of the along-track gradient of $\mu_{\rm TRUE}$
$V_{\boldsymbol{M}_{\rm E}}(t)$	Radar voltage sample for point $\boldsymbol{M}_{\rm E}$ at time t
$K_{\rm PP,1}$	Lag-1 pulse-pair (PP) correlation function for 1 burst of CPR pulses
$(Z_{\rm PP,1}, \mu_{\rm PP,1})$	Single-burst PP Doppler moments estimates
$N_{\rm integ}$	Number of consecutive burst groups that are integrated
$K_{\rm PP}$	Lag-1 pulse-pair (PP) correlation function for $N_{\rm integ}$ burst groups
$(Z_{\rm PP}, \mu_{\rm PP})$	$N_{\rm integ}$-burst PP Doppler moments estimates
$K_{\rm TRUE}$	$K_{\rm PP}$ simulated without spacecraft-induced broadening
K	$K_{\rm PP}$ after NUBF correction of Eq. (6)
$\kappa_{\rm NUBF}$	Correlation coefficient between NUBF bias and $\nabla_x Z_{\rm PP}$
$\mathcal{K},\ \mathcal{K}_{\rm TRUE}$	Along-track Fourier transforms of K and $K_{\rm TRUE}$
Δf	Spectral sampling step $[\mathrm{km}^{-1}]$
$\mathcal{A},\ \mathcal{B}$	Ranges of the filter parameters α and β
$\mathcal{L}_{\alpha,\beta}$	Transfer function of low-pass filter of parameters (α, β)
$\Theta_{\alpha,\beta}$	Spectral bandwidth $[\mathrm{km}^{-1}]$ of $\mathcal{L}_{\alpha,\beta}$
$X_{\alpha,\beta} = [2\Theta_{\alpha,\beta}]^{-1}$	Spatial scale [km] of $\mathcal{L}_{\alpha,\beta}$
$\mathcal{K}_{\alpha,\beta}$	Spectrum $\mathcal{K}$ filtered using $\mathcal{L}_{\alpha,\beta}$
$K_{\alpha,\beta}$	Inverse Fourier transform of $\mathcal{K}_{\alpha,\beta}$
$\mu_{\alpha,\beta}$	Filtered velocity $[\mathrm{m}\cdot\mathrm{s}^{-1}]$ obtained by PP processing of $K_{\alpha,\beta}$
$E_{\alpha,\beta}$	Filtered-velocity error $[\mathrm{m}\cdot\mathrm{s}^{-1}]$ with respect to $\mu_{\rm TRUE}$
$R_{\alpha,\beta}$	Filtered-velocity residue $[\mathrm{m}\cdot\mathrm{s}^{-1}]$
$E_{\rm PRE}$	Pre-filtering velocity error $[\mathrm{m}\cdot\mathrm{s}^{-1}]$ with respect to $\mu_{\rm TRUE}$
$f_{E_{\rm PRE}},\ f_{E_{\alpha,\beta}},\ f_{R_{\alpha,\beta}}$	Probability density function (pdfs) of $E_{\rm PRE}$, $E_{\alpha,\beta}$ and $R_{\alpha,\beta}$
$F_{R_{\alpha,\beta}}$	Cumulative distribution function (cdf) of $R_{\alpha,\beta}$
$\widehat{f}_{E_{\rm PRE}}, \widehat{f}_{E_{\alpha,\beta}}$	Estimates of $f_{E_{\rm PRE}}$ and $f_{E_{\alpha,\beta}}$
$\widehat{F}_{E_{\rm PRE}-E_{\alpha,\beta}}$	Estimated cdf of $E_{\rm PRE} - E_{\alpha,\beta}$
$f_{\rm ERR}$	Estimate of $f_{E_{\rm PRE}}$ using $\mu_{\rm PP}$ and assuming $\mu_{\rm TRUE}$ is known
$f_{\rm ANA}$	Analytical approximation of $f_{E_{\rm PRE}}$
$\mathcal{I}$	Set of filter parameters that lead to $E_{\alpha,\beta}$ *statistically independent* from $E_{\rm PRE}$
$\mathcal{I}_{\rm E},\ \mathcal{I}_{\rm A}$	Estimates of $\mathcal{I}$ using $f_{E_{\rm PRE}}$ or $f_{\rm ANA}$
$T(\alpha, \beta)$	Kolmogorov-Smirnov (KS) statistic of $F_{R_{\alpha,\beta}}$ and $\widehat{F}_{E_{\rm PRE}-E_{\alpha,\beta}}$
$N_{\alpha,\beta} = X_{\alpha,\beta}/(T_{\rm S} V_{\rm SAT})$	Number of voltage samples used to obtain one random realization of $E_{\alpha,\beta}$.

APPENDIX A
DISTRIBUTION OF THE FILTERED VELOCITY ERROR $E_{\alpha,\beta}$

The list of symbols is presented in Table VI.

Given a filter $\mathcal{L}_{\alpha,\beta}$, the distribution $f_{E_{\alpha,\beta}}$ is approximated by generating an ensemble of realizations of the random process $E_{\alpha,\beta}$. This is done by simulating equivalent (I, Q) voltage samples that represent the effect of the filter.

1) We start by determining the range $D_{\rm SNR} = [\mathrm{SNR}_{lo}, \mathrm{SNR}_{hi}]$ of SNR for which the statistics of the velocity are computed. The pdf $f_{\rm SNR}$ of the SNR is also computed. The pdf of $E_{\alpha,\beta}$ can be then expressed as a mixture density as follows:

$$f_{E_{\alpha,\beta}}(v) = \int_{D_{\rm SNR}} f_{\rm SNR}(s_0) f_{E_{\alpha,\beta}}(s_0, v)\, ds_0, \quad \forall\, v \in \mathbb{R} \quad (26)$$

in which $f_{E_{\alpha,\beta}}(s_0, \cdot)$ is the conditional pdf of $E_{\alpha,\beta}$ knowing $\mathrm{SNR} = s_0$.

2) To approximate $f_{E_{\alpha,\beta}}(s_0, \cdot)$ for any z_0 in $D_{\rm SNR}$, a so-called "error Doppler spectrum" is simulated. This spectrum has a total area equal to s_0, a mean equal to $\mu_0 = 0\ \mathrm{m}\cdot\mathrm{s}^{-1}$ and a width consistent with EC-CPR's specifications, which is analytically computed. A Doppler broadening $\sim 1\ \mathrm{m}\cdot\mathrm{s}^{-1}$ is added to the spacecraft-induced broadening to account for moderate turbulence and the spread in terminal velocities [11]. The thus obtained analytical estimate of the spectral width is constant for the entire scene. Although the spectral width of EC-CPR does not change much, it is sensitive to the turbulence broadening. Hence, instead of a constant analytical value, one could consider using pointwise PP estimates of the spectral width, which will be an EC-CPR product [10]. However, one has to weigh the accuracy of this estimate,

which is noisy, versus the variability of turbulence. Moreover, due to the nonlinear dependence of the (I, Q) samples on Doppler width, one would need to simulate new sequences of (I, Q) samples for each point. This would pose a significant challenge to the computational efficiency of the filters and is therefore not considered in the scope of this paper.

3) The EC-CPR (I, Q) resulting from the error Doppler spectrum are random and temporally sampled at the rate of EC-CPR's PRF. These (I, Q) samples are horizontally integrated over a distance $X_{\alpha,\beta} = [2\Theta_{\alpha,\beta}]^{-1}$, which corresponds to the scale of $\mathcal{L}_{\alpha,\beta}$, where the bandwidth $\Theta_{\alpha,\beta}$ is defined in (24). Thus, $N_{\alpha,\beta} = X_{\alpha,\beta}/(T_{\rm S}V_{\rm SAT})$ voltage samples are used in the PP processing to obtain one random realization of $E_{\alpha,\beta}$. By repeating this process $N_{\rm stats}$ times, an ensemble of $N_{\rm stats}$ velocity error estimates is obtained, from which $f_{E_{\alpha,\beta}}(s_0, \cdot)$ can be evaluated. In our simulations, we use $N_{\rm stats} = 500$.
4) This process is applied to all the values of SNR s_0 in $D_{\rm SNR}$, and the resulting set of distributions is mixed according to (26) to obtain $f_{E_{\alpha,\beta}}$.

To reduce the computational cost of this approach, the integral in (26) is approximated by a discrete sum, e.g., using a trapezoidal rule. Furthermore, given an SNR s_0, rather than simulating new (I, Q) samples for every (α, β) in $\mathcal{A} \times \mathcal{B}$, we first simulate a large data set that contains $N_{\rm stats}N_{\rm max}$ samples, where $N_{\rm max} = \max_{(\alpha,\beta)\in\mathcal{A}\times\mathcal{B}} N_{\alpha,\beta}$. Despite the size of this data set, the advantage is that it has to be evaluated *only once*. Then, for every filter $\mathcal{L}_{\alpha,\beta}$, a subset of $N_{\rm stats}N_{\alpha,\beta}$ voltage samples is used to determine the $N_{\rm stats}$ realizations of $E_{\alpha,\beta}$ at s_0 and, therewith, the pdf $f_{E_{\alpha,\beta}}(s_0, \cdot)$.

APPENDIX B
DISTRIBUTION OF THE PREFILTERING VELOCITY ERROR $E_{\rm PRE}$

An analytical approximation of $f_{E_{\rm PRE}}$ is obtained by applying the method described in Appendix A. In this case, the along-track integration is performed over 500 m to achieve the level-1B sampling, i.e., using $N_{500} = {\rm floor}[500/(T_{\rm S}V_{\rm SAT})]$ voltage samples if $T_{\rm S}V_{\rm SAT}$ is expressed in meters. The resulting approximation of $f_{E_{\rm PRE}}$ is denoted $f_{\rm ANA}$.

APPENDIX C
CONSTRAINED MAXIMUM ENTROPY FILTERS

Similarly to the constrained filters that minimize the variance of the residue, one can also consider maximizing the entropy of the residue over the search space. Thus, once the space $\mathcal{I}_{\rm A}$ has been determined using $f_{\rm ANA}$ in (23), the optimal "constrained residue entropy maximizing" (REA) filter is defined as

$$(\alpha_{\rm REA}, \beta_{\rm REA}) = \underset{(\alpha,\beta)\in\mathcal{I}_{\rm A}}{\arg\max}\ S\,[R_{\alpha,\beta}]. \tag{27}$$

The general statistics of this REA filter, which are provided in Table VII, show that the REA filter produces results that are almost identical to those of the RVA filter and, therefore, nearly optimal. Hence, the REA filter is an alternative and equivalent implementation that can be considered for the adaptive matched filtering.

TABLE VII
ALTERNATIVE CONSTRAINED FILTERS: MAXIMUM ENTROPY FILTERS (REA), MINIMUM RESIDUE VARIANCE FILTERS CONSTRAINED BY UNCORRELATEDNESS (RVUA), AND SURFACE-BASED FILTERS (RVS, RES, AND RVUS)

General statistics (SNR $\geq$ 6)		SPIDER simulations			WACR simulations		
	PRF [kHz]	6.1	7	7.5	6.1	7	7.5
$\sigma(E_u)$ [m · s^{-1}]	u = pre	1.58	1.18	1.02	1.45	1.04	0.90
	u = EVM	0.53	0.42	0.38	0.35	0.29	0.27
	u = REM	1.15	0.65	0.53	0.94	0.46	0.36
	u = RVA	0.59	0.49	0.47	0.39	0.35	0.35
	u = REA	0.58	0.49	0.44	0.38	0.35	0.33
	u = RVUE	0.59	0.51	0.47	0.37	0.36	0.37
	u = RVUA	0.66	0.70	0.66	0.46	0.55	0.51
	u = RVS	0.61	0.51	0.43	-	-	-
	u = RES	0.61	0.51	0.43	-	-	-
	u = RVUS	0.67	0.54	0.49	-	-	-
$\sigma(E_{\rm PP})$ [m · s^{-1}] after along-track integration	1 km	1.07	0.76	0.63	0.99	0.71	0.60
	5 km	0.78	0.71	0.70	0.61	0.53	0.52
	10 km	0.84	0.82	0.82	0.61	0.56	0.57

APPENDIX D
OPTIMIZATION CONSTRAINED BY UNCORRELATEDNESS

In Section IV-C3, the optimization was constrained by enforcing the independence between the prefiltering and filtered velocity errors $E_{\alpha,\beta}$ and $E_{\rm PRE}$, respectively. A looser assumption could be made to arrive at (20) by requiring that $E_{\alpha,\beta}$ and $E_{\rm PRE}$ be mutually *statistically uncorrelated*. This amounts to restricting $\mathcal{A} \times \mathcal{B}$ to the set $\mathcal{U}$ of filter parameters such that

$$\sigma^2[R_{\alpha,\beta}] = \sigma^2[E_{\rm PRE}] + \sigma^2[E_{\alpha,\beta}], \quad \text{for any } (\alpha,\beta) \in \mathcal{U}. \tag{28}$$

Therefore, the optimal *"residue variance minimizing filter constrained by uncorrelatedness" (RVU)* is obtained by solving

$$(\alpha_{\rm RVU}, \beta_{\rm RVU}) = \underset{(\alpha,\beta)\in\mathcal{U}}{\arg\min}\ \sigma^2\,[R_{\alpha,\beta}]. \tag{29}$$

The search space $\mathcal{U}$ for the RVU filter is determined by finding the parameters (α, β) that minimize the difference between $\sigma^2[R_{\alpha,\beta}]$ and an estimate of the right-hand side of (28), i.e.,

$$\mathcal{U} = \left\{(\alpha,\beta) \in \mathcal{A}\times\mathcal{B}, \left|\sigma^2[R_{\alpha,\beta}] - \sigma^2[\widehat{E}_{\rm PRE}] - \sigma^2[\widehat{E}_{\alpha,\beta}]\right| \leq V_{\max}\right\} \tag{30}$$

with $V_{\max} \geq 0$ a threshold value. The term $\sigma^2[\widehat{E}_{\alpha,\beta}]$ is the variance of $\widehat{f}_{-E_{\alpha,\beta}}$, which is defined in Appendix A, whereas $\sigma^2[\widehat{E}_{\rm PRE}]$ represents either the variance of $f_{\rm ERR}$ (RVUE filter), which assumes the knowledge of $\mu_{\rm TRUE}$, or the variance of the analytical pdf $f_{\rm ANA}$ (RVUA filter).

The results obtained with these filters are also listed in Table VII. The accuracy of the RVUE results confirms that the optimization can indeed be constrained by uncorrelatedness

rather than independence. However, this type of optimization is highly sensitive to the accuracy of the estimate of $\sigma^2[\widehat{E}_{\rm PRE}]$, as highlighted by the suboptimal RVUA results due to the fact that $f_{\rm ANA}$ is NUBF free. Hence, by using the entire distribution of the residue rather than its variance only, the assumption of independence in the RVA approach leads to an optimization that is more robust to the imperfections of the NUBF corrections than the assumption of uncorrelatedness.

APPENDIX E
CONSTRAINED OPTIMIZATIONS USING THE SURFACE RETURN

In the constrained optimization algorithm described in Appendix B, instead of approximating $f_{E_{\rm PRE}}$ analytically with $f_{\rm ANA}$, one can take advantage of the Doppler measurements from the surface. Indeed, provided that the true vertical velocity at the surface vanishes, the measured $\mu_{\rm PP}$ at the surface actually represents a velocity error that is readily available. The corresponding distribution of surface velocities, which is denoted $f_{\rm SFC}$, can be then used as a surrogate for $f_{E_{\rm PRE}}$. To avoid areas where the surface Doppler data are strongly attenuated by precipitation of clouds aloft, $f_{\rm SFC}$ is derived using only the surface points above which the average reflectivity factor does not exceed the threshold -10 dBZ. Evidently, approximating $f_{E_{\rm PRE}}$ by $f_{\rm SFC}$ is a first-order approximation that does not capture the entire variability of the velocity error versus the SNR since the surface SNR is significantly larger than the typical values of atmospheric SNR [10].

Using $f_{\rm SFC}$, and similarly to the RVA, REA, and RVUA filters, the following three surface-based filters are built, viz., 1) a minimum residue variance (RVS) filter constrained by independence, 2) a maximum residue entropy (RES) filter constrained by independence, and 3) a minimum residue variance filter constrained by uncorrelatedness (RVUS). The performances of these filters on the SPIDER data set are summarized in Table VII (these filters cannot be applied to the WACR data, due to the absence of surface return in the input ground-based measurements).

Interestingly, the use of the surface return yields also accurate results. Both the RVS and RES filters produce results that are similar to the analytical RVA and REA filters. Moreover, with regard to the filters based on uncorrelatedness, the RVUS filter outperforms the RVUA filter and reaches the accuracy of the RVUE filter, built using the actual velocity error. This feature stems from the fact that the surface velocity is also affected by some uncompensated NUBF biases, which, in turn, affects the shape and width of $f_{\rm SFC}$ unlike $f_{\rm ANA}$.

Despite these encouraging results for the usability of the surface return to build the matched filters, a finer analysis must be conducted to assess the sensitivity of the matched filters to the differences in SNR and turbulence regimes between the surface and the atmospheric velocities.

ACKNOWLEDGMENT

The research described in this paper was carried out at the Jet Propulsion Laboratory, California Institute of Technology, under a contract with the National Aeronautics and Space Administration. The authors would like to thank the NASA Stand Alone Mission of Opportunity Notice/U.S. Participating Investigator program for the support. They would also like to thank the reviewers for their constructive remarks.

REFERENCES

[1] S. Kobayashi, H. Kumagai, and H. Kuroiwa, "A proposal of pulse-pair Doppler operation on a spaceborne cloud-profiling radar in the W band," *J. Atmos. Ocean. Technol.*, vol. 19, no. 9, pp. 1294–1306, Sep. 2002.

[2] D. S. Zrnic, "Spectral moment estimates from correlated pulse pairs," *IEEE Trans. Aerosp. Electron. Syst.*, vol. 13, no. 4, pp. 344–354, Jul. 1977.

[3] R. Meneghini and T. Kozu, *Spaceborne Weather Radar*. Norwood, MA, USA: Artech House, 1990.

[4] S. Tanelli, E. Im, S. L. Durden, L. Facheris, D. Giuli, and E. A. Smith, "Rainfall Doppler velocity measurements from spaceborne radar: Overcoming nonuniform beam-filling effects," *J. Atmos. Ocean. Technol.*, vol. 21, no. 1, pp. 27–44, Jan. 2004.

[5] N. A. J. Schutgens, "Simulated Doppler radar observations of inhomogeneous clouds: Application to the EarthCARE space mission," *J. Atmos. Ocean. Technol.*, vol. 25, no. 1, pp. 26–42, Jan. 2008.

[6] S. Tanelli, E. Im, S. Kobayashi, R. Mascelloni, and L. Facheris, "Spaceborne Doppler radar measurements of rainfall: Correction of errors induced by pointing uncertainties," *J. Atmos. Ocean. Technol.*, vol. 22, no. 11, pp. 1676–1690, Nov. 2005.

[7] A. Battaglia, T. Augustynek, S. Tanelli, and P. Kollias, "Multiple scattering identification in spaceborne W-band radar measurements of deep convective cores," *J. Geophys. Res. Atmos.*, vol. 116, no. D19, pp. 19201-1–19201-12, Oct. 2011.

[8] O. Sy, S. Tanelli, N. Takahashi, Y. Ohno, H. Hiroaki, and P. Kollias, "Simulation of EarthCARE spaceborne Doppler radar products using ground-based and airborne data: Effects of aliasing and non-uniform beam-filling," *IEEE Trans. Geosci. Remote Sens.*, vol. 52, no. 2, pp. 1463–1479, Feb. 2014.

[9] P. Kollias, S. Tanelli, A. Battaglia, and A. Tatarevic, "Evaluation of EarthCARE cloud profiling radar Doppler velocity measurements in particle sedimentation regimes," *J. Atmos. Ocean. Technol.*, vol. 31, no. 2, pp. 366–386, Feb. 2014.

[10] R. Doviak and D. Zrnic, *Doppler Radar and Weather Observations*, 2nd ed. New York, NY, USA: Academic, 1993.

[11] P. W. Sloss and D. Atlas, "Wind shear and reflectivity gradient effects on Doppler radar spectra," *J. Atmos. Sci.*, vol. 25, no. 6, pp. 1080–1089, Nov. 1968.

[12] M. P. Wand and M. C. Jones, *Kernel Smoothing*, 1st ed. London, U.K.: Chapman & Hall, 1994.

[13] D. Sirmans and B. Bumgarner, "Numerical comparison of five mean frequency estimators," *J. Appl. Meteorol.*, vol. 14, no. 6, pp. 991–1003, Sep. 1975.

[14] G. Haase and T. Landelius, "Dealiasing of Doppler radar velocities using a torus mapping," *J. Atmos. Ocean. Technol.*, vol. 21, no. 10, pp. 1566–1573, Oct. 2004.

[15] A. Battaglia and S. Tanelli, "DOMUS: DOppler multiple-scattering simulator," *IEEE Trans. Geosci. Remote Sens.*, vol. 49, no. 1, pp. 442–450, Jan. 2011.

[16] A. Uematsu, Y. Ohno, K. Sato, H. Kumagai, and H. Horie, "Simulation of Doppler velocity measurement performance for EarthCARE spaceborne cloud profiling radar," in *Proc. 5th Eur. Conf. Radar Meteorol. Hydrol.*, 2008.

[17] H. Horie, T. Iguchi, H. Hanado, H. Kuroiwa, H. Okamoto, and H. Kumagai, "Development of a 95-GHz airborne cloud profiling radar (SPIDER)—Technical aspects," *IEICE Trans. Commun.*, vol. E83-B, no. 9, pp. 2010–2020, 2000.

[18] G. Turin, "An introduction to matched filters," *IRE Trans. Inf. Theory*, vol. 6, no. 3, pp. 311–329, Jun. 1960.

[19] A. Papoulis, *Probability, Random Variables and Stochastic Processes*. New York, NY, USA: McGraw-Hill, 1991.

[20] K. Widener and J. Mead, "W-band ARM cloud radar specifications and design," in *Proc. 14th ARM Sci. Team Meet. Proceedings, Albuquerque*, Albuquerque, NM, USA, Mar. 22–26, 2004, pp. 1–6.

[21] H. Nakatsuka, H. Horie, K. Okada, Y. Sakaide, T. Kimura, Y. Ohno, K. Sato, N. Takahashi, and H. Kumagai, "Development status of cloud profiling radar for EarthCARE," in *Proc. Conf. Series SPIE*, Sep. 2009, vol. 7474, pp. 74740O-1–74740O-8.

Ousmane O. Sy received the Ingénieur degree and the PEGASUS certificate in aerospace engineering from École Nationale de l'Aviation Civile, Toulouse, France, the M.Sc. degree (*cum laude*) in microwaves and optical telecommunications from Paul Sabatier University, Toulouse, and the Ph.D. degree in stochastic electromagnetics from the Eindhoven University of Technology, Eindhoven, The Netherlands, in 2003 and 2009, respectively.

He participated in the thermal vacuum campaign of Eutelsat's 7A telecommunications satellite in 2003. From 2004 to 2005, he was with Airbus as a Test Engineer on aeronautical navigation systems. From 2009 to 2012, he was a Caltech Postdoctoral Researcher with the NASA/Caltech Jet Propulsion Laboratory (JPL), Pasadena, CA, USA, where he has been a Visiting Assistant Researcher affiliated with the UCLA Joint Institute for Regional Earth System Science and Engineering since December 2012. His current research interests include retrieval algorithms for spaceborne, airborne, and ground-based weather radars; Doppler radars; computational electromagnetics; and stochastic uncertainty quantification.

Dr. Sy was a recipient of a certificate of appreciation from the IEEE student branch in Eindhoven in 2008, a Young Scientist award during the general assembly of the International Union of Radio Science in Chicago in 2008, and the first prize at the Student Paper competition of Zürich's international symposium on electromagnetic compatibility held in Switzerland in 2009.

Simone Tanelli received the Laurea and Ph.D. degrees in electronics engineering and remote sensing from the University of Florence, Florence, Italy, in 1995 and 1999, respectively.

He has been with the Jet Propulsion Laboratory, Pasadena, CA, USA, since 2001. He is a Lead Radar Operations Engineer for CloudSat's Cloud Profiling Radar, a Member of the CloudSat and GPM algorithm development working groups and the PMM Science Team, and a Co-Lead of the Radar Studies Group for the ACE Science Working Group. He has also served as an invited expert for the EarthCARE Joint Mission Advisory Group. He has been involved in scientific research and technology development for cloud and precipitation radars and other remote sensing instruments.

Pavlos Kollias was born in Athens, Greece, in 1971. He received the B.Sc. degree in physics and the M.Sc. degree in environmental physics from the University of Athens, Athens, in 1994 and 1996, respectively, and the Ph.D. degree in meteorology from the University of Miami, Miami, FL, USA, in 2000.

He is currently an Associate Professor and a Canada Research Chair in Radar Application in Weather and Climate Research with the Department of Atmospheric and Oceanic Sciences, McGill University, Quebec, Canada. He is an international leader in the application of short-wavelength radars for cloud and precipitation research from ground- and space-based platforms. He is a member of the Mission Advisory Group and the algorithm development team of the European Space Agency Earth Cloud, Aerosol and Radiation Explorer Mission. He has authored or coauthored over 70 scientific articles in peer-reviewed literature in the areas of millimeter-wavelength radar research, cloud, and precipitation physics.

Yuichi Ohno received the M.S. degree in atmospheric science from Kyoto University, Kyoto, Japan, in 1988.

Since 1988, he has been a Researcher with the Communications Research Laboratory (renamed National Institute of Information and Communications Technology, 2004), Tokyo, Japan. He is involved in meteorological research using millimeter-wave cloud radar and the development of spaceborne cloud profiling radar for the Earth Cloud, Aerosol and Radiation Explorer Mission mission.